205

CALCULATION OF THE NEUTRON SOURCE DISTRIBUTION IN THE VENUS PWR ENGINEERING MOCK-UP EXPERIMENT

A Thesis

Submitted to the Graduate Faculty of the
Louisiana State University and
Agricultural and Mechanical College
in partial fulfillment of the
requirements for the degree of
Master of Science

in

The Department of Nuclear Engineering

by
Paul Olufemi Morakinyo
B.A.Sc., University of Windsor, 1980
M.S., Louisiana State University, 1982
May 1984

DEDICATED TO

my family

ACKNOWLEDGEMENT

I have been aided by a number of people and organizations during the process of this study. I especially wish to acknowledge my deep indebtedness to my major professor, Dr. Mark L. Williams, who provided me with invaluable technical assistance and encouragement throughout the course of this study. I am also grateful to the personnel of CEN/SCK in Mol, Belgium for providing the experimental measurements and other necessary data which enabled the goals of this study to be realized. The contributions of L. Leenders, G. Minsart, and A. Fabry are especially appreciated. Special thanks are also due to the staff of Oak Ridge National Laboratory for making their computer available for a great portion of this study and also for their overall cooperation and assistance.

I also wish to express my gratitude to Dr. John C. Courtney, who recommended me for this study. My appreciation goes to the entire faculty and staff of the Nuclear Science Center for the various ways in which they have assisted me during my studies at the Center.

This study was funded by the United States Nuclear Regulatory Commission, and was made possible through grants from the Engineering Physics Division of Oak Ridge National Laboratory to the Nuclear Science Center at Louisiana State University.

TABLE OF CONTENTS

LIST OF TABLES

LIST OF TABLES (Continued)

LIST OF FIGURES

LIST OF FIGURES (Continued)

ABSTRACT

The neutron fission source distribution in the core of the VENUS PWR Mock-up Experiment is computed and compared to experimental measurements. This experiment is an important component of the United States Nuclear Regulatory Commission's (USNRC's) program goal of benchmarking reactor pressure vessel (RPV) fluence calculations in order to determine the accuracy to which RPV damage can be computed. Of particular concern is the accuracy of the source calculation near the core-baffle interface, which is the important region for contributing to RPV fluence.

Calculations were performed with two-dimensional discrete ordinates transport theory, using cross-sections based on ENDF/B-IV data. In addition to in-core fission rate calculations, several ex-core fission chamber responses were computed. The accuracy of the calculations were evaluated by comparison with the experimental measurements.

Results indicate that the calculated neutron source distribution within the VENUS core agrees with the experimental measured values with an average error of less than 3%. At the important core-baffle interface, the

agreement is within 3% error, except at the baffle corner, where the error is about 6%. The ex-core results are also in good agreement with measurements, except at the circular steel barrel, which was approximated into a rectangular geometry. It was discovered that a better accuracy in the calculations can be obtained by applying a detailed space dependent cross-section weighting procedure to the core-baffle interface region. It is concluded that by using this cross-section weighting in a two-dimensional transport theory calculation of the source distribution in a well-defined LWR core, the maximum error introduced into the predicted RPV fluence due to source errors should be on the order of 5%. However, in power reactor analysis, additional uncertainties (such as the time-dependent core composition and the use of few group diffusion theory) could affect this value somewhat.

Chapter I

INTRODUCTION

The long-term potential for neutron embrittlement of reactor vessels has been a recognized concern of the nuclear industry for a number of years[1]. Recognition of pressurized water reactor (PWR) transients that could lead to severe thermal shock to the reactor pressure vessel (RPV), and the increasing awareness that some older plants are accumulating radiation damage at a faster rate than originally predicted have resulted in a re-evaluation of the RPV integrity during postulated overcooling accidents[2].

There are indications that, under certain conditions, some postulated overcooling accidents could possibly result in pressure vessel failure, particularly if the transients occur late in the operating life of the vessel[2]. Although the probability of such occurrences is small, the consequences are catastrophic, hence the net risk is not negligible. Of particular concern are several older reactors which contain large amounts of copper and nickel in the RPV welds. These reactor vessels are more susceptible to radiation embrittlement, whereby the ductile to brittle transition temperature of the vessel material is shifted to a higher temperature[3]. Injection of emergency core coolant

in the core and other events that allow cool water to come in contact with the inner surface of the RPV could theoretically lower the RPV temperature below the nil ductility transition temperature. The rapid cooling of the inner surface at a time when the primary system pressure is substantial results in high RPV stresses, which, when coupled with reduction in the fracture toughness near the inner surface, introduces the possibility of propagation of pre-existent inner surface flaws. This possibility increases with reactor operating time because of an additional reduction in fracture toughness that is the result of neutron exposure.

In March 1982, the United States Nuclear Regulatory Commission (USNRC) offically declared the problem referred to as "pressurized thermal shock (PTS)" to be an unresolved safety issue.

To evaluate RPV integrity for both PTS and end of life (EOL) considerations, the need and importance of an accurate determination of the damage fluence accumulated by the RPV cannot be over-emphasized. Towards this end, the USNRC and the nuclear industry are currently conducting studies to determine the ability of PWR vessels to withstand severe thermal shocks without compromising their integrity. One of the major components of the USNRC research consists of benchmarking RPV fluence determination methods, since the

RPV fluence is a main factor in the degree of radiation embrittlement.

An important part of the on-going RPV benchmark studies called "the VENUS PWR Engineering Mock-up Experiment" is being performed at the Louisiana State University (LSU) Nuclear Science Center. This experiment is one of a series of experiments which have been performed at various research reactors to validate particular aspects of RPV fluence calculations. A large number of the earlier experiments were performed at the Pool Critical Assembly (PCA), the Oak Ridge Research Reactor Pool Side Facility (ORR-PSF), and the Bulk Shielding Reactor (BSR), all of which are located at the Oak Ridge National Laboratory (ORNL).

While these earlier experiments are useful in benchmarking the accuracy of ex-core transport calculations, they did not address the problem of determining the core fission source distribution, which drives the RPV fluence calculation. Of particular concern is the accuracy of the source calculation near the core-baffle interface, which is the important region for contributing to RPV fluence. The PWR Engineering Mock-up Experiment was designed primarily to address this problem. The experimental work is being performed by CEN/SCK ("Centre d'Etude de L'energie Nucleaire/Studie Centrum voor Kern energie") at the VENUS Critical Facility in Mol, Belgium, while the calculational

study is being done by both Mol and the LSU Nuclear Science Center in cooperation with ORNL.

The primary objective of this study is to accurately determine the VENUS core neutron source distribution, and compare with measured values in order to contribute to USNRC's program goal of benchmarking RPV fluence calculations. Upon satisfactory agreement, the calculated fission source will be used in a later study as a fixed source for ex-core calculations. In addition to in-core measurements, U-235 and Np-237 fission chamber (dosimetry) measurements have been obtained and compared with ex-core calculations.

In summary, the purpose of this thesis is to achieve the following goals:

1. Generate a few group cross-sections that have been accurately weighted for the VENUS benchmark configuration. These cross-sections will be available for future VENUS core calculations.
2. Perform discrete ordinates transport calculations to determine the neutron source at each point in the VENUS core.
3. Examine the behavior of the thermal neutron flux near the core-baffle interface to determine the adequacy of a single thermal group.
4. Validate the accuracy of the calculational method by comparing the results with benchmark measurements.

5. Analyze the discrepancies associated with the results, and recommend procedures to improve the accuracy of the calculational methods for determining the core neutron source used in RPV fluence calculations.
6. Provide the neutron source results for subsequent use in calculating the transport of neutrons from the VENUS core to the RPV, thereby establishing the RPV damage fluence.

The end results of this thesis will contribute to the overall PTS analysis program by validating the accuracy of the neutron source calculation in PWR cores which drives the determination of the RPV fluence. Uncertainties in the source distribution contribute to the uncertainty in the estimated vessel damage, which in turn results in an uncertainty in the ability of the RPV to withstand PTS transients.

Chapter II

EXPERIMENTAL CONFIGURATION

II.1 VENUS Description

The PWR benchmark configuration in the VENUS Critical Facility is shown in Fig. II-1. The central portion of the geometry is water, surrounded by a 2.858 cm thick inner steel baffle. The inner core zone in the immediate vicinity of the inner baffle contains 752 zircaloy-clad 3.3% enriched fuel cells, with 48 pyrex rods interspersed among them. The outer core zone contains 1800 steel-clad 4.0% enriched fuel cells. The core itself is surrounded by a 2.858 cm thick outer steel baffle, a water reflector, a 4.972 cm thick steel core barrel, a water gap, a neutron pad, and the reactor pool.

The configuration shown in Fig. II-1 was selected by Mol as the core loading best suited for the realization of the required measurements in the fuel zones, reflector, barrel, and up to the neutron pad. The distribution of pyrex rods in the inner zone of the core permits criticality without boron in water and it shifts the power peak towards the core edges, thereby improving the core power distribution for the ex-core measurements. In addition, the

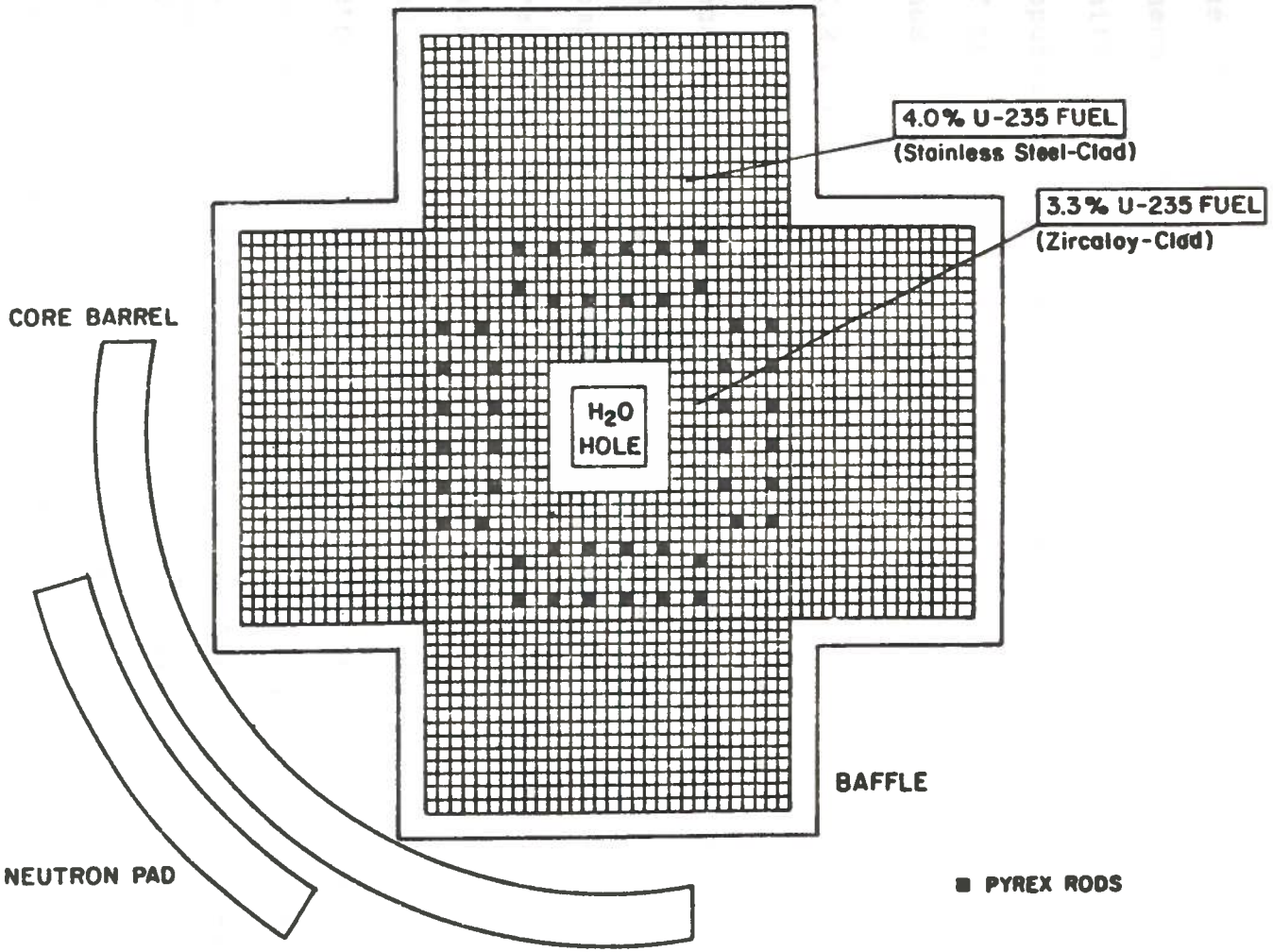

Fig. II-1. VENUS Benchmark Configuration.

use of water in the core center provides an interior zone of thermal neutrons for additional measurements, and it also shifts power towards the core edge. The 4.0% fuel pins (as opposed to the 3.3% fuel pins) were placed in the outer zone of the core to increase the fast flux levels in the pad, thus facilitating accurate measurements[4].

II.2 VENUS Specifications

The characteristics of the fuel cells and the pyrex rods used in the VENUS benchmark configuration are specified in Table II-1 and II-4 respectively. The chemical composition of the materials contained in the configuration are shown in Tables II-2, II-3, II-5, II-6, and II-7. The material specifications are considered to be very accurate, and were obtained by Mol using sophisticated and detailed methods.[5] Much effort has been devoted to insuring that this experiment is well characterized and of benchmark quality. It is possible that experimental results (e.g. the power distribution and criticality) for this exercise could be quite beneficial to other reactor physics benchmarking efforts (e.g. cross-section data testing) that are not directly related to the PTS study.

Table II-1. Characteristics of the Fuel Cells Used in the VENUS Configuration

Characteristics		4.0% U-235 Enriched Fuel	3.3% U-235 Enriched Fuel
Stoichiometry:	(o/U+Pu)	2.000 ± 0.010	1.997 ± 0.005
Chemical composition of fuel (w/o)	UO_2	100.0	100.0
	PuO_2	0.0	0.0
Isotopic composition of uranium (w/o)	U-234	0.031 ± 0.009	0.029 ± 0.001
	U-235	4.022 ± 0.008	3.306 ± 0.010
	U-236	0.023 ± 0.006	0.016 ± 0.001
	U-238	95.924 ± 0.010	96.649 ± 0.012
Lattice pitch (cm):		1.260	1.260
Fuel diameter(cm):		0.8926 ± 0.0005	0.819 ± 0.002
Fuel length (cm):		50.0 ± 0.5	50.0 ± 0.1
Linear specific weight of fuel (gm/cm):		6.39 ± 0.07	5.40 ± 0.05
Cladding material:		SS-304	Zircaloy-4
Cladding internal diameter (cm):		0.902 ± 0.004	0.836 ± 0.001
Cladding external diameter (cm):		0.978 ± 0.002	0.950 ± 0.001
Linear specific weight of cladding (gm/cm):		0.8855 ± 0.0007	1.0627 ± 0.0004
Number of available fuel cells:		1800	752

Table II-2. Chemical Composition of SS-304 Cladding for the 4.0% Fuel Type

SS-304 Elements	Chemical Composition (w/o)	Atomic Weight* (gm)
C	0.04 ± 0.04	--
Mn	1.29 ± 0.03	54.938
P	0.02 ± 0.02	--
S	0.015 ± 0.003	--
Si	0.135 ± 0.003	--
Cr	18.3 ± 0.4	51.996
Ni	10.03 ± 0.20	58.71
Mo	0.132 ± 0.003	--
Fe	70.038 ± 0.711	55.847

* Atomic weights are given for only the important elements.

Table II-3. Chemical Composition of Zircaloy-4 Cladding for the 3.3% Fuel Type

Zircaloy-4 Elements	Chemical Composition (w/o)	Atomic Weight* (gm)
Fe	0.20 ± 0.01	--
Cr	0.10 ± 0.01	--
Sn	1.41 ± 0.06	118.69
O	0.12 ± 0.01	--
Zr	98.17 ± 0.06	91.22

* Atomic weights are given for only the important elements.

Table II-4. Characteristics of the Pyrex Rods Used in the VENUS Configuration

Pyrex material:		Corning glass code 7740
Chemical composition (w/o):	SiO_2	78.53
	B_2O_3	14.65 ± 0.15
	Al_2O_3	2.21
	Fe_2O_3	0.05
	Na_2O_3	3.44
	K_2O_3	1.13
Isotopic composition of boron (a/o):	B-10	19.775 ± 0.005
	B-11	80.225 ± 0.005
Lattice pitch (cm):		1.260
Pyrex inner diameter(cm):		0.6058 ± 0.0031
Pyrex outer diameter (cm):		0.9048 ± 0.0045
Pyrex length (cm):		50.0 ± 0.1
Linear specific weight of pyrex (gm/cm):		0.7886 ± 0.0052
Cladding material:		SS-304
Cladding inner diameter (cm):		0.940 ± 0.003
Cladding outer diameter (cm):		0.978 ± 0.005
Specific weight of cladding (gm/cm^3):		7.9 ± 0.1
Number of available pyrex rods:		48

Table II-5. Chemical Composition of SS-304 Cladding for the Pyrex Rod

SS-304 Elements	Chemical Composition (w/o)	Atomic Weight* (gm)
C	0.03 ± 0.03	--
Mn	0.87 ± 0.42	54.938
Si	0.29 ± 0.16	--
Cr	18.4 ± 0.1	51.996
Ni	9.5 ± 0.5	58.71
Mo	0.07 ± 0.07	--
Fe	70.84 ± 1.28	55.847

* Atomic weights are given for only the important elements.

Table II-6. Chemical Composition of SS-304 Baffle

SS-304 Elements	Chemical Composition (w/o)	Atomic Weight* (gm)
C	0.04 ± 0.04	--
Mn	1.371 ± 0.441	54.938
P	0.022 ± 0.022	--
S	0.015 ± 0.015	--
Si	0.213 ± 0.040	--
Cr	16.37 ± 0.23	51.996
Ni	8.72 ± 0.15	58.71
Mo	0.457 ± 0.076	--
Fe	72.745 ± 0.343	55.847
Co	0.047 ± 0.070	--

* Atomic weights are given for only the important elements.

Table II-7. Chemical Composition of SS-304 Barrel

SS-304 Elements	Chemical Composition (w/o)	Atomic Weight* (gm)
C	0.015	--
Mn	1.303 ± 0.430	54.938
P	0.028	--
S	0.005	--
Si	0.513	--
Cr	18.464 ± 0.200	51.996
Ni	10.199 ± 0.380	58.71
Mo	0.474	--
Fe	68.819 ± 1.010	55.847
Co	0.097	--
N	0.080	--

* Atomic weights are given for only the important elements.

Chapter III

OVERVIEW OF CALCULATIONS

The procedural steps employed in calculating the space dependent neutron source within the VENUS core are outlined below:

1. Determination of Reactor Parameters

   Using the given specifications, the atom densities of all important nuclides encountered in the core are calculated. Other reactor parameters such as dimensions, buckling, etc. are also determined, based on specifications provided by Mol. These values are given in Appendix C.

2. Fine-Group Cross-Section Library

   A 218 neutron group cross-section library[6] based on ENDF/B-IV nuclear data is used. The problem-independent cross-section library contains a total of 65 different nuclides, which encompasses all the necessary materials in the reactor.

3. Energy Self Shielding Calculation

   For each resonance nuclide encountered in the fuel region of the heterogeneous lattice unit cell, the flux in the absorber region is calculated with the Nordheim

integral method. This weighting function is used to average the cross-section of the resonance nuclide, in order to account for resonance shielding effects. This is discussed in Section IV.2.

4. Spatial Self Shielding (or Cell-Averaging) Calculation

The disadvantage factor associated with the resonance shielded cross-section in the fuel region is calculated, and used to spatially average the group cross-section over a unit cell. This is discussed in Section IV.2.

5. Collapse of Fine-Group Cross-Sections

The fine-group (218) cell-averaged cross-sections are collapsed into a broad group (10) structure, using a calculated spectrum to flux weight the cross-section. This is discussed in Section IV.3.

6. Eigenvalue Calculation

Using the broad-group cross-sections, the total neutron source distribution is determined from a k-eigenvalue calculation of the VENUS core, with the neutron flux normalized consistently with the experimental normalization. This is discussed in Chapter V.

7. Fixed Source Calculations

The neutron source distribution obtained from the eigenvalue calculation is used to perform a 56 group fixed source calculation. This is discussed in Chapter V.

The overall calculations for the determination of the neutron source distribution in the VENUS configuration is summarized in the flow chart of Fig. III-1.

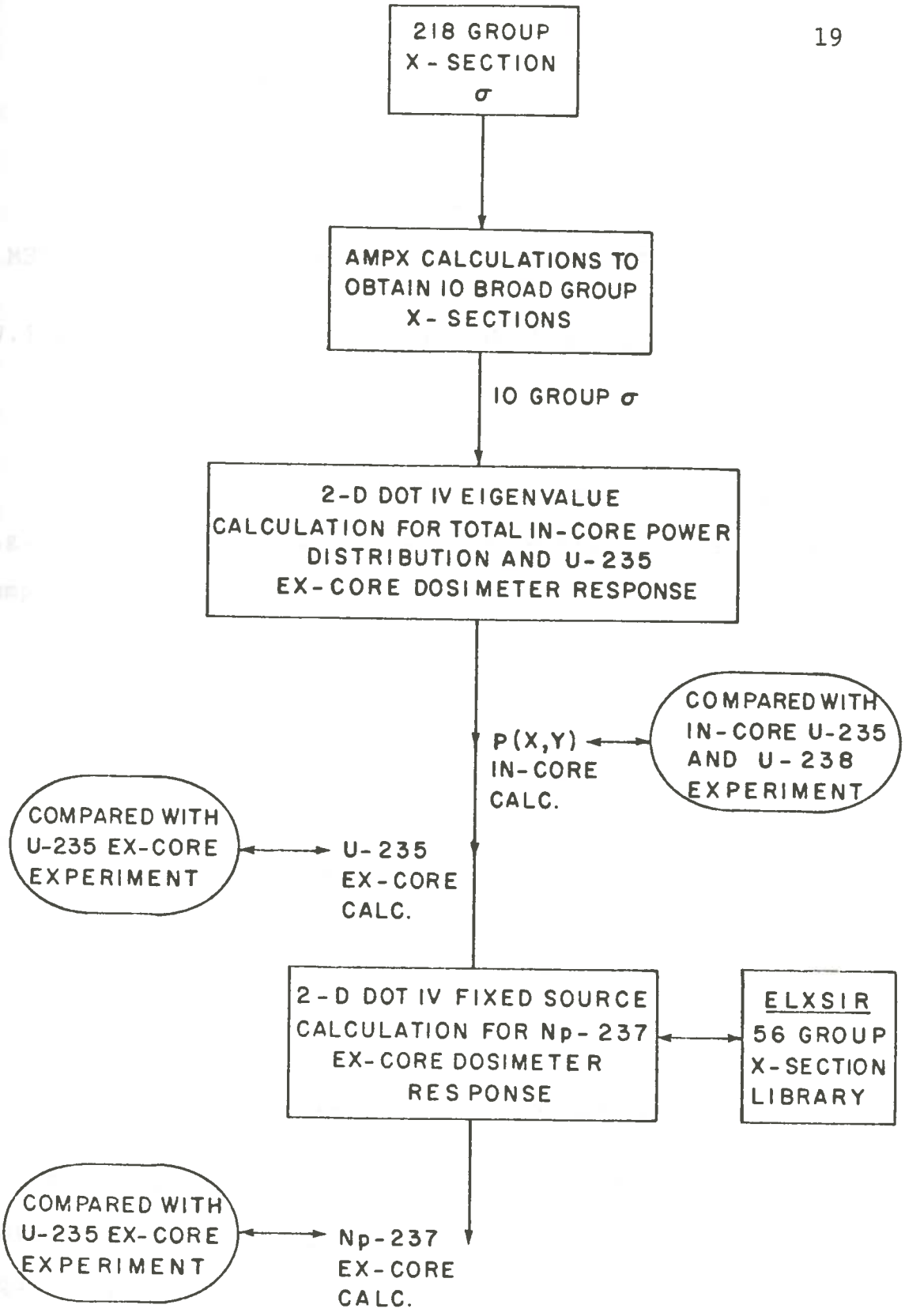

Fig. III-1. Flow Chart of the Overall Calculations.

Chapter IV

METHODOLOGY FOR PROCESSING GROUP DEPENDENT CROSS-SECTIONS

IV.1 Derivation of Cell-Averaged Multigroup Cross-Section Equation

Cell Theory

Consider a unit cell in the VENUS core lattice. Fig. IV-1 shows a unit cell with a centrally located fuel lump surrounded by a moderator.

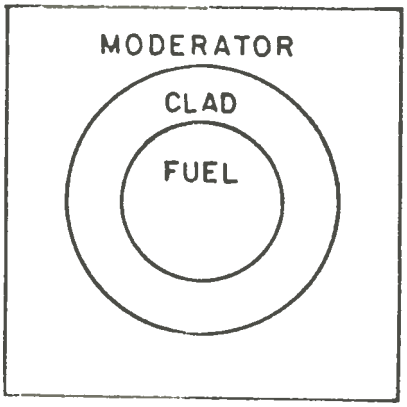

Fig. IV-1. A Unit Fuel Cell.

The unit cell is heterogeneous, but it has three homogenized regions, namely the fuel, clad, and moderator. Consequently, we can determine the "equivalent homogenized" parameters spatially constant over the cell. These homo-

genized parameters will be equivalent in the sense that they will reproduce the average reaction rates throughout the cell. In essence, we are seeking "equivalent" group parameters that are constant over the volume occupied by any given cell making up the core, and that when used in energy dependent transport calculation for the whole core, will reproduce the same average reaction rates over a given cell for the reactor, with heterogeneous geometrical characteristics of all cells treated explicitly.

Cell-Averaged Equation

In order to account for localized pin heterogeneities, it is necessary that the core materials be cell-averaged. From cell theory†, the reaction rate in a cell is computed with cell-averaged cross sections defined to preserve the true reaction rate, i. e.

$$\bar{\Sigma}^i_{c,g}\,\bar{\Phi}_{c,g}\,V_c = \int_{V_F}\int_g \Sigma^i_F(E)\Phi(r,E)\,dE\,dV + \int_{V_M}\int_g \Sigma^i_M(E)\Phi(r,E)\,dE\,dV \qquad \text{(IV-1)}$$

where: $\bar{\Sigma}^i_{c,g}$ ≡ cell-averaged macroscopic cross-section for group g of the i-th nuclide in the cell

$\bar{\Phi}_{c,g}$ ≡ cell-averaged flux for group g

---

† For simplicity, the clad region is neglected in this discussion. The results can easily be generalized to three regions.

V_c ≡ cell volume

$\Sigma_F^i(E)$, $\Sigma_M^i(E)$ ≡ energy dependent macroscopic cross-sections of the i-th nuclide in the fuel and moderator respectively

$\Phi(r,E)$ ≡ space and energy dependent flux

Multiplying the first-term on the R.H.S.of Eq. (IV-1)

by $\frac{V_F}{V_F}$, and then by $\frac{\int_g \bar{\Phi}_F(E)dE}{\int_g \bar{\Phi}_F(E)dE}$, we have:

$$\int_{V_F}\int_g \Sigma_F^i(E)\Phi(r,E)dEdV = V_F \int_g \Sigma_F^i(E) \frac{\int_{V_F}\Phi(r,E)dV}{V_F} dE$$

$$= V_F \int_g \Sigma_F^i(E)\,\bar{\Phi}_F(E)dE$$

$$= V_F \frac{\int_g \Sigma_F^i(E)\,\bar{\Phi}_F(E)dE}{\int_g \bar{\Phi}_F(E)dE} \int_g \bar{\Phi}_F(E)dE$$

$$= V_F\, \bar{\Sigma}_{F,g}^{i}\, \bar{\Phi}_{F,g} \qquad \text{(IV-2)}$$

where: $\bar{\Sigma}_{F,g}^{i}$ ≡ value of the cross-section averaged over the fuel lump (and <u>not</u> over the entire unit cell) for group g

$$= \frac{\int_g \Sigma_F^i(E)\,\bar{\Phi}_F(E)dE}{\int_g \bar{\Phi}_F(E)dE}$$

$\bar{\Phi}_{F,g}$ ≡ flux averaged over the fuel lump for group g

In a similar manner, the second-term on the R.H.S. of Eq. (IV-1) can be expressed as:

$$\int_{V_M} \int_g \Sigma_M^i(E)\ \Phi(r,E)dEdV = V_M\ \bar{\Sigma}_{M,g}^i\ \bar{\Phi}_{M,g} \qquad \text{(IV-3)}$$

Substituting Eqs. (IV-2) and (IV-3) into Eq. (IV-1), we have:

$$\bar{\Sigma}_{c,g}^i\ \bar{\Phi}_{c,g}\ V_c = \bar{\Sigma}_{F,g}^i\ \bar{\Phi}_{F,g}\ V_F + \bar{\Sigma}_{M,g}^i\ \bar{\Phi}_{M,g}\ V_M \qquad \text{(IV-4)}$$

Notice that:

$$V_c = V_F + V_M \qquad \text{(IV-5)}$$

where: $V_F \equiv$ volume of the fuel region

$V_M \equiv$ volume of the moderator region

The R.H.S. of Eq. (IV-4) can be written in terms of microscopic cross-sections as shown below:

$$\bar{\Sigma}_{c,g}^i\ \bar{\Phi}_{c,g}\ V_c = N_F^i\ \bar{\sigma}_{F,g}^i\ \bar{\Phi}_{F,g}\ V_F + N_M^i\ \bar{\sigma}_{M,g}^i\ \bar{\Phi}_{M,g}\ V_M \qquad \text{(IV-6)}$$

where: N_F^i, $N_M^i \equiv$ atom densities of the i-th nuclide in the fuel and moderator respectively

$\bar{\sigma}_{F,g}^i$, $\bar{\sigma}_{M,g}^i \equiv$ average microscopic cross-sections of the i-th nuclide for group g in the fuel and moderator respectively

Rearranging Eq. (IV-6) to solve for $\bar{\Sigma}_{c,g}^i$, we have:

$$\bar{\Sigma}^i_{c,g} = N^i_F \bar{\sigma}^i_{F,g} \frac{\bar{\Phi}_{F,g}}{\bar{\Phi}_{c,g}} \frac{V_F}{V_c} + N^i_M \bar{\sigma}^i_{M,g} \frac{\bar{\Phi}_{M,g}}{\bar{\Phi}_{c,g}} \frac{V_M}{V_c} \qquad \text{(IV-7)}$$

It can be seen from Eq. (IV-7) that in order to obtain the cell-averaged cross-section $\bar{\Sigma}^i_{c,g}$, it is necessary to know the zone-averaged cross-sections $\bar{\sigma}^i_{F,g}$, $\bar{\sigma}^i_{M,g}$, and the

flux ratios $\frac{\bar{\Phi}_{F,g}}{\bar{\Phi}_{c,g}}$, $\frac{\bar{\Phi}_{M,g}}{\bar{\Phi}_{c,g}}$.

Each flux ratio is called advantage or disadvantage factor, depending on whether it is greater or less than unity, respectively.

IV.2 Energy and Spatial Self Shielding

Nuclides with resonance effects are usually associated with materials in the fuel region. The complexity of the heterogeneous lattice treatment stems from the fact that the flux in the resonance region is a function of both energy and space. To account for localized pin heterogenieties, it becomes necessary that the core materials be resonance shielded and cell-averaged.

Energy Self Shielding - NITAWL

Essentially, the fuel group cross-sections ($\bar{\sigma}^i_{F,g}$)

associated with the first term on the R.H.S. of Eq. (IV-7) must be resonance shielded, as implied by Eq. (IV-2).

By averaging the actual data over the various energy groups, with the scalar flux as a weighting function, we can compute the shielded, problem dependent cross-sections, i.e.

$$\bar{\sigma}^{i}_{F,g} = \frac{\int_{g}^{g-1} \bar{\Phi}_F(E)\sigma^{i}(E)dE}{\int_{g}^{g-1} \bar{\Phi}_F(E)dE} \qquad \text{(IV-8)}$$

where: $(g, g-1) \equiv$ energy interval of the g-th energy group

$\sigma^{i}(E) \equiv$ actual cross-section data for nuclide i

$\bar{\Phi}_F(E) \equiv$ energy dependent flux for weighting (to be computed)

In the resonance energy range, $\bar{\Phi}_F(E)$ and $\sigma^{i}(E)$ may both vary drastically, and the flux weighting, referred to as "energy self shielding (or resonance shielding)" is most important.

The scalar flux of Eq. (IV-8) was determined for each fuel type by using the Nordheim[7] integral method, which basically solves an expression for the collision density in the fuel lump. The Nordheim integral treatment solves the integral slowing down equation for the energy dependent flux

in a material region that contains a resonance absorber (i.e. fuel lump) and a maximum of two admixed moderators. The presence of more than one absorber in the moderating region (i.e. a fuel pin lattice) is accounted for through the use of a Dancoff-Ginsberg correction factor. The collision density equation solved by the Nordheim method can be written as:

$$\Sigma_{tF}(E)\,\bar{\Phi}_F(E) = \sum_{i=1}^{3}\left[\frac{1-P^{*}_{Fo}(E)}{1-\alpha_F^i}\int_E^{E/\alpha_F^i}\Sigma^i_{SF}(E')\,\bar{\Phi}_F(E')\,\frac{dE'}{E'} + \frac{P^{*}_{FO}(E)\,\Sigma^i_{tF}(E)}{\overline{\xi\Sigma}_s\;E}\right] \qquad \text{(IV-9)}$$

where: $\Sigma_{tF}(E) \equiv$ total macroscopic cross-section of the fuel at energy E

$\bar{\Phi}^i_F(E) \equiv$ average flux in the fuel at energy E

$i \equiv$ nuclide index:

i = 1 for the absorber

i = 2 for the first admixed moderator in the fuel

i = 3 for the second admixed moderator in the fuel

$\alpha_F^i \equiv \left(\frac{A_F^i-1}{A_F^i+1}\right)^2$, $A_F^i \equiv$ mass of the i-th nuclide contained in the fuel region

$P^{*}_{FO}(E) \equiv$ Dancoff-Ginsberg corrected first-flight escape probability for the abosorber region

$\Sigma^i_{sF}(E')$ ≡ macroscopic scattering cross-section of the i-th nuclide colliding in the fuel region at energy E'

$\bar{\Phi}_F(E')$ ≡ average flux in the fuel at energy E'

$\Sigma^i_{tF}(E)$ ≡ total macroscopic cross-section of the i-th nuclide in the fuel region at energy E

$\bar{\xi}$ ≡ average logarithmic energy decrement

$\bar{\Sigma}_s$ ≡ average macroscopic moderator scattering cross-section

The Nordheim's method is implemented in the NITAWL[8,9] code, where each resonance is treated independently. For each resonance the flux in the absorber region is obtained by numerical integration over a fine energy mesh (of lethargy intervals), with slowing down sources due to the absorber and the two admixed moderators explicitly calculated as in Eq. (IV-9). Having determined the scalar flux for each fuel type, the shielded (resolved) cross-sections represented by Eq. (IV-8) are subsequently calculated. Details of the Nordheim integral treatment, and its implementation in NITAWL can be found in Appendix A.

Spatial Self Shielding (Cell-Averaging) - XSDRNPM

The energy shielded cross-section can be used to homogenize the unit cell by multiplying by the associated flux

ratios $\frac{\Phi_{F,g}}{\Phi_{c,g}}$ and $\frac{\Phi_{M,g}}{\Phi_{c,g}}$ of Eq. (IV-7).

A multiplication of the energy shielded cross-section by the flux ratio constitute spatial self shielding of the cross-section (or spatial cross-section weighting).

The flux ratios were calculated with a one-dimensional discrete ordinates code called XSDRNPM[10]. This code numerically solves the time-independent Boltzmann equation in one-dimension with the coordinate system of interest. Details of the one-dimensional discrete ordinates method and its implementation in XSDRNPM can be found in Appendix B.

The square unit cell was modeled into a cylindrical Wigner-Seitz unit cell of mixtures and zones with appropriate spatial intervals. The cylindrical geometries for the 3.3%, and 4.0% fuel types, and for the pyrex rod are shown in Figs. IV-2, IV-3, and IV-4, respectively. In the XSDRNPM weighting calculation, the "cell weighting" option was used for the fuel cells, while the "inner cell weighting" option was used for the pyrex rod. The XSDRNPM calculations were based on S8-P3 approximation.

IV.3 Cross-Section Collapsing

After cell homogenization, the XSDRNPM code was again used to perform a one-dimensional, 218 group transport

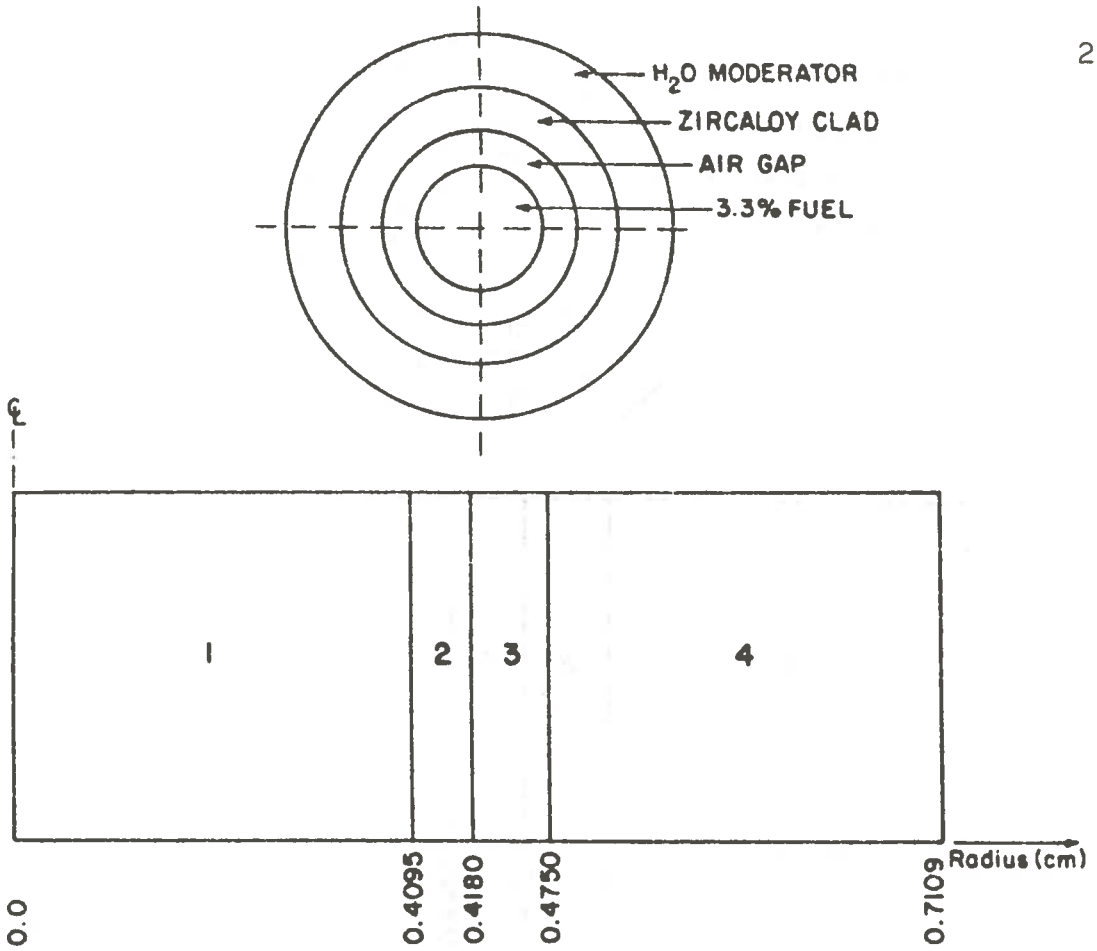

Definition:

Zone	Composition	# of Spatial Intervals
1	3.3% Fuel Pellet	10
2	Air Gap	1
3	Zircaloy Clad	1
4	H_2O Moderator	10

Fig. IV-2. 3.3% Fuel Cell Geometry for Cross-Section Averaging.

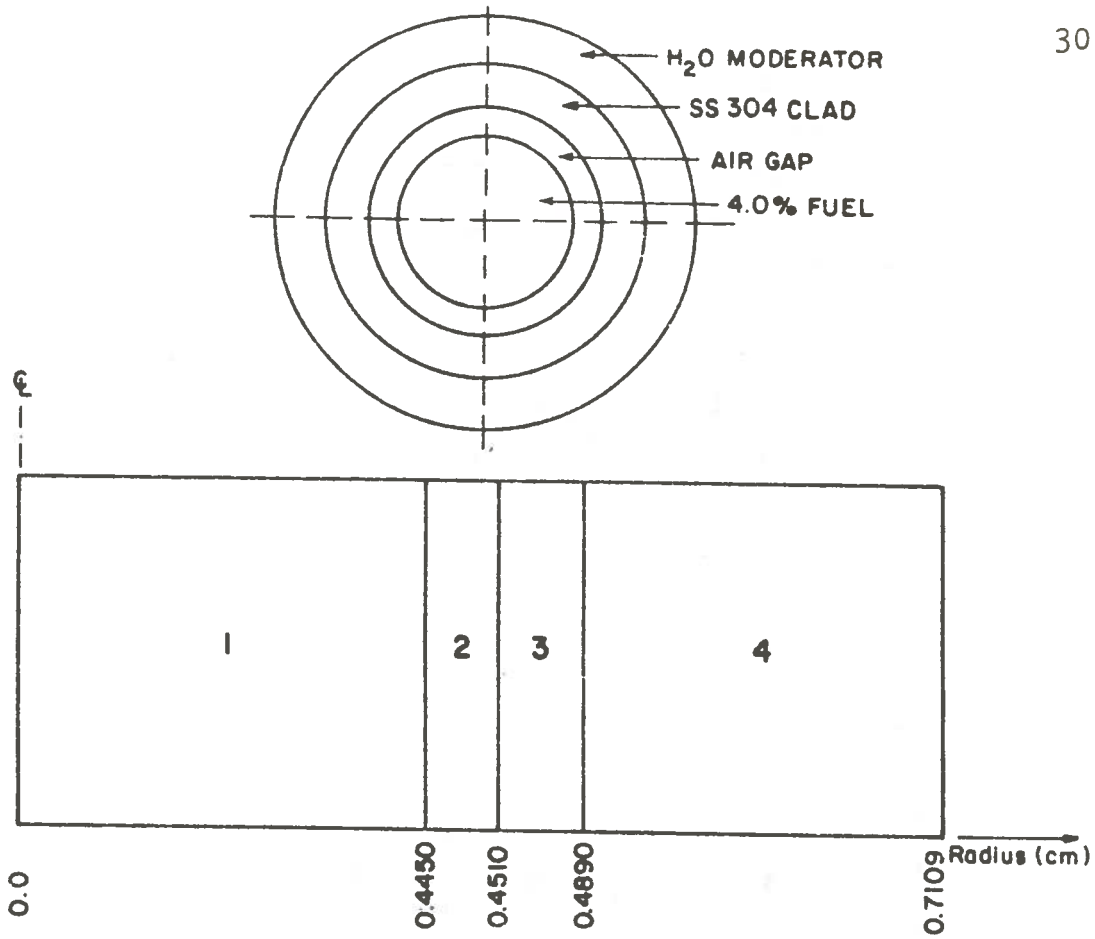

Definition:

Zone	Composition	# of Spatial Intervals
1	4.0% Fuel Pellet	10
2	Air Gap	1
3	SS-304 Clad	1
4	H_2O Moderator	10

Fig. IV-3. 4.0% Fuel Cell Geometry for Cross-Section Averaging.

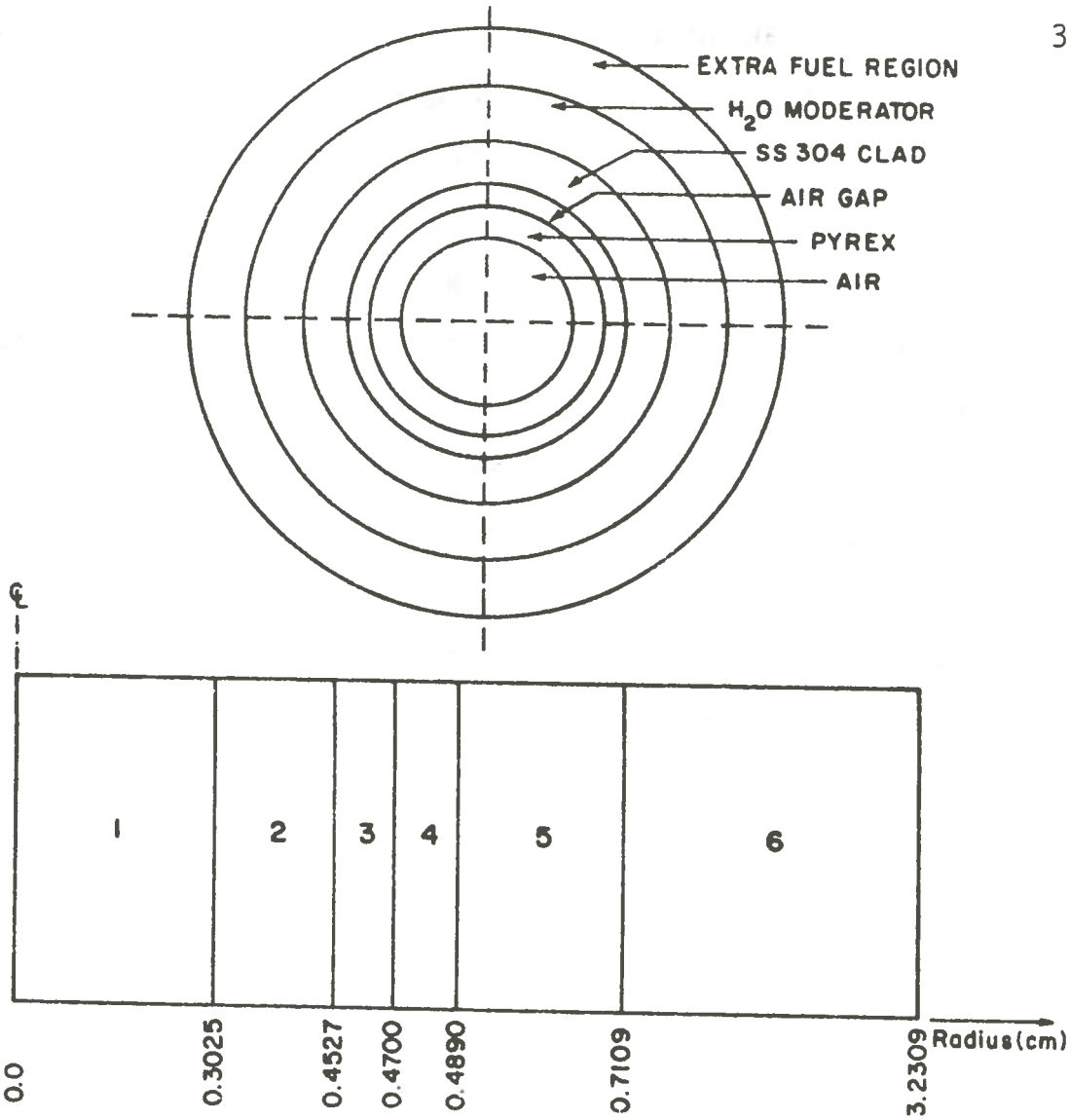

Definition:

Zone	Composition	# of Spatial Intervals
1	Air	10
2	Pyrex	5
3	Air Gap	1
4	SS-304 Clad	1
4	H_2O Moderator	10
6	Extra Fuel Region	30

Fig. IV-4. Pyrex Cell with Extra Fuel Cell Geometry for Cell Calculation.

theory calculation in order to obtain zone weighting spectra. Fig. IV-5 corresponds to the one-dimensional cylindrical model of the VENUS configuration used in the calculation. The weighting spectra were then used to zone-wise collapse the 218 fine-group cross-section into 10 broad groups, with the energy boundaries of Table IV-1. The 218 group cross-sections contain 78 thermal groups, which permit an accurate calculation of the thermal spectrum used in averaging the single thermal group of the 10 group structure. It should be noted that the single inner 3.3% and the seven outer 4.0% zones of Fig. IV-5 are boundary zones, which have been used to account for the change in the thermal spectrum near the core-baffle interfaces.

The expression for the collapsed zone dependent broad group cross-section can be written as:

$$\overline{\Sigma}_{c,G}(Z) = \frac{\sum_{g\varepsilon G} \overline{\Sigma}_{c,g}\, \overline{\Phi}_g(Z)}{\sum_{g\varepsilon G} \overline{\Phi}_g(Z)} \qquad \text{(IV-10)}$$

where $\overline{\Phi}_g(Z)$ is a zone weighted spectrum calculated from the one-dimensional model of the VENUS configuration, g is the fine-group index, and G is the broad-group index.

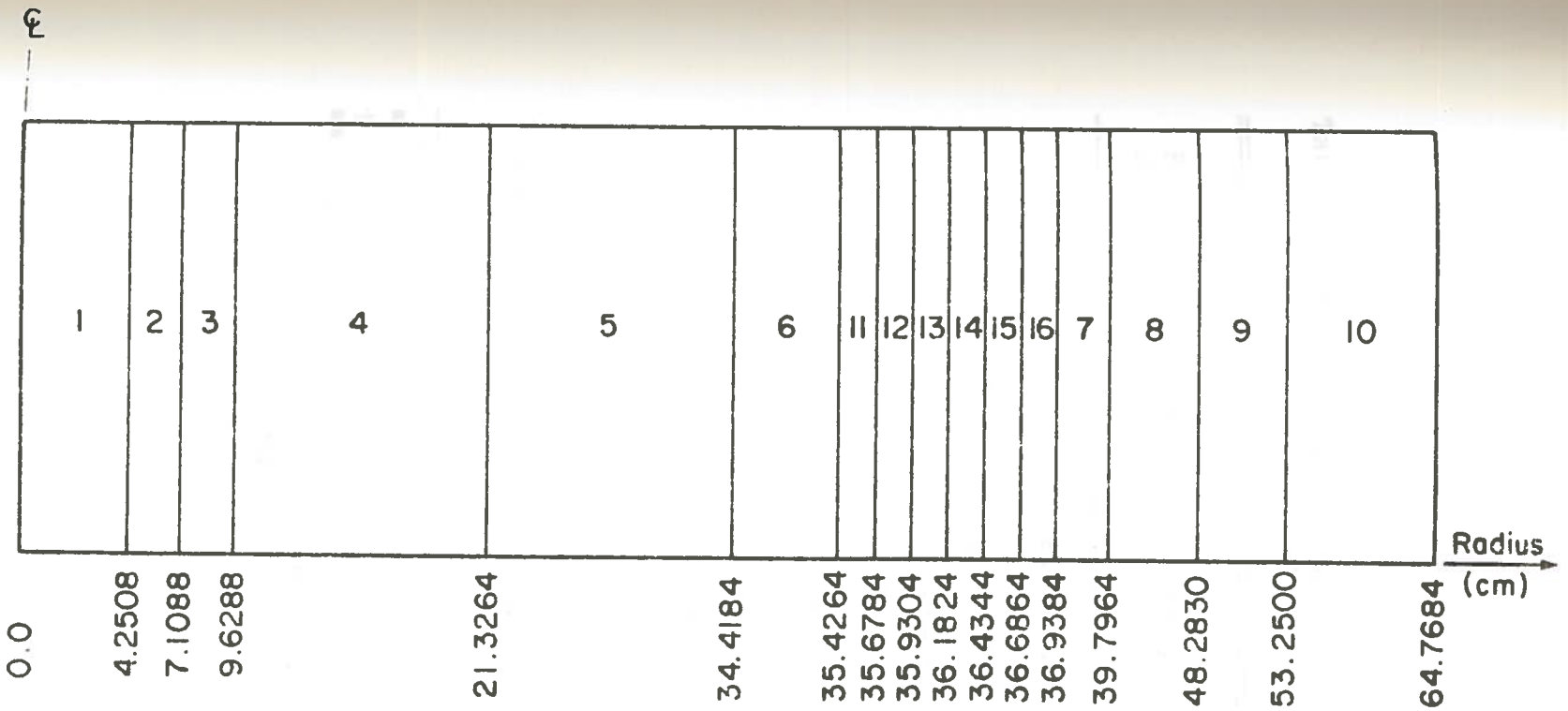

Definition:

Zone	Description	Composition	# of Spatial Intervals
1	Water Hole	Water	15
2	Inner Baffle	SS-304	10
3	Inner 3.3% Fuel	3.3% Fuel + Pyrex	10
4	outer 3.3% Fuel	3.3% Fuel + Pyrex	22
5	Inner 4.0% Fuel	4.0% Fuel	25
6	Outer 4.0% Fuel	4.0% Fuel	4
7	Outer Baffle	SS-304	10
8	Reflector	Water	22
9	Simulated Barrel	SS-304	10
10	Water Pool	Water	12
11-16	Outer 4.0% Fuel	4.0% Fuel	6

Fig. IV-5. 1-D Cylindrical Model of the VENUS Configuration.

Table IV-1. 10 Group Energy Structure used in the 2-D Eigenvalue Calculation

Broad Group	Fine Groups	Upper Energy (eV)	Lower Lethargy	Fission Spectrum**
1	1-7	2.00E+07	-0.6931	4.250E-01
2	8-33	1.85E+06	1.6870	5.137E-01
3	34-46	2.70E+05	3.6120	5.876E-02
4	47-53	3.00E+04	5.8090	2.407E-03
5	54-66	3.90E+03	7.8490	1.135E-04
6	67-83	5.50E+02	9.8080	6.055E-06
7	84-124	7.20E+01	11.8400	2.856E-07
8	125-154	1.00E+01	13.8200	1.434E-08
9	155-191	1.86E+00	15.5000	9.921E-10
10*,†	192-218	6.50E-01	16.5500	2.583E-10

* Lower energy of group 10 = 1.00E-05 eV.
† Upper lethargy of group 10 = 27.63.
** This is an ENDF/B-IV fission spectrum resulting from the ENDF/B-IV cross-section data. An ENDF/B-V based fission spectrum was used in the 2-D calculation, for better accuracy.

IV.4 Flow Chart of Calculations

The AMPX[11] modular system was used for all the cross-section processing calculations. The AMPX system is a collection of computer programs in a modular arrangement for processing cross-section data. The modularity is particularly attractive, since it allows the user to choose an arbitrary execution sequence from the modules available in the system. Details of the AMPX system can be found in Reference 11.

A flow chart of the various AMPX modules used in the cross-section processing calculations is shown in Fig. IV-6.

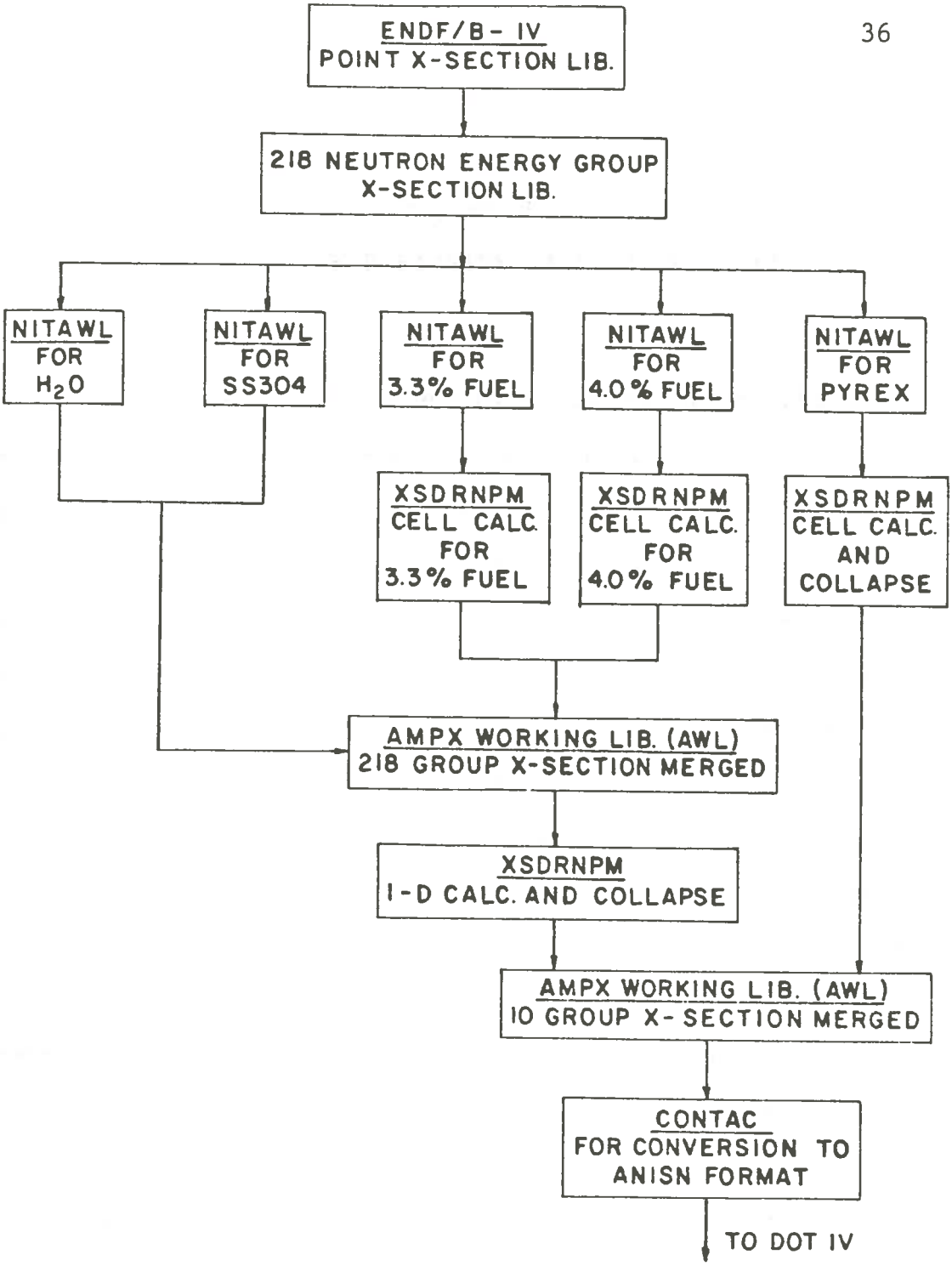

Fig. IV-6. Flow Chart of AMPX Modules for X-Section Processing.

Chapter V

METHODOLOGY FOR FISSION RATE CALCULATION

V.1 Eigenvalue Calculation

The total fission source distribution in the VENUS core was determined from a k-eigenvalue calculation of the reactor core. The Dot IV[12] code was used to perform a two-dimensional X-Y calculation of the critical eigenvalue. DOT IV is a two-dimensional discrete ordinates code which numerically solves the Boltzmann transport equation. The Boltzmann equation, which is a mathematical expression of the neutron-balance condition, is solved for the flow of neutrons moving in a set of discrete directions in each interval of a space mesh, and in each group of a multigroup energy structure. Since the neutron balance condition must be maintained over an arbitrary spatial region, energy interval, and discrete direction, DOT IV produces an accounting of the various production and loss mechanism within a specified zone or region.

A two dimensional form of the the Boltzmann transport equation solved by DOT IV in rectangular coordinates can be expressed as:

$$\Omega_x \frac{\partial}{\partial x}[\psi(x,y,E,\Omega)] + \Omega_y \frac{\partial}{\partial y}[\psi(x,y,E,\Omega)] + \sum_t(x,y,E)\psi(x,y,E,\Omega)$$

$$= \int_{E'} \int_{\Omega'} \sum_s(x,y,E'\rightarrow E,\Omega'\rightarrow\Omega)\ \psi(x,y,E',\Omega')d\Omega'dE'$$

$$+ S(x,y,E,\Omega) + Q(x,y,E,\Omega)$$

where: Ω_x, Ω_y ≡ direction cosines of the unit direction vector Ω, = $\vec{i}.\Omega$ and $\vec{j}.\Omega$ respectively

$\psi(x,y,E,\Omega)$, $\psi(x,y,E',\Omega')$ ≡ angular fluxes

$\sum_t(x,y,E)$ ≡ total macroscopic cross-section

$\sum_s(x,y,E'\rightarrow E,\Omega'\rightarrow\Omega)$ ≡ angular dependent scatter cross-section for a neutron of energy E' in direction Ω' scattering into energy E in direction Ω

$S(x,y,E,\Omega) = \chi(E) \int_{E'} \int_{\Omega'} \nu \sum_f(x,y,E')\ \psi(x,y,E',\Omega')d\Omega'dE'$

≡ fission source

$Q(x,y,E,\Omega)$ ≡ fixed (or external) source

$\chi(E)$ ≡ fission spectrum

ν ≡ average number of neutrons per fission

$\sum_f(x,y,E')$ ≡ macroscopic fission cross-section

Details of the DOT IV code can be found in Appendix B.

For the two-dimensional calculation, the VENUS benchmark configuration was modeled in X-Y rectangular coordinates since the fuel cells are loaded in a rectangular pitch. Due to the fact that this is a core calculation, the model was terminated at the core barrel. The fact, that rectangular coordinate were used, required that the circular steel barrel be approximated as a "stair-step." The model used in the two-dimensional calculations is shown in Fig. V-1. The model was divided into zones as shown in Fig. V-2, and the corresponding descriptions are given in Table V-1. Notice that as in the one-dimensional model, boundary zones have been included at the inner and outer core boundaries in order to use the appropriately weighted cross-sections.

Before the DOT IV calculation was performed, the 10 group microscopic cross-section obtained earlier was combined into the appropriate macroscopic mixture cross-section, using the cell homogenized atom density values of Table V-2.

The DOT IV eigenvalue was performed with a P_3 Legendre expansion of the cross sections and an S_8 quadrature set. The weighted flux differencing scheme was used and the calculation was accelerated with the diffision acceleration option. The VENUS model, as shown in Figs. V-1 and V-2 contains 103 mesh intervals in both the X and Y directions.

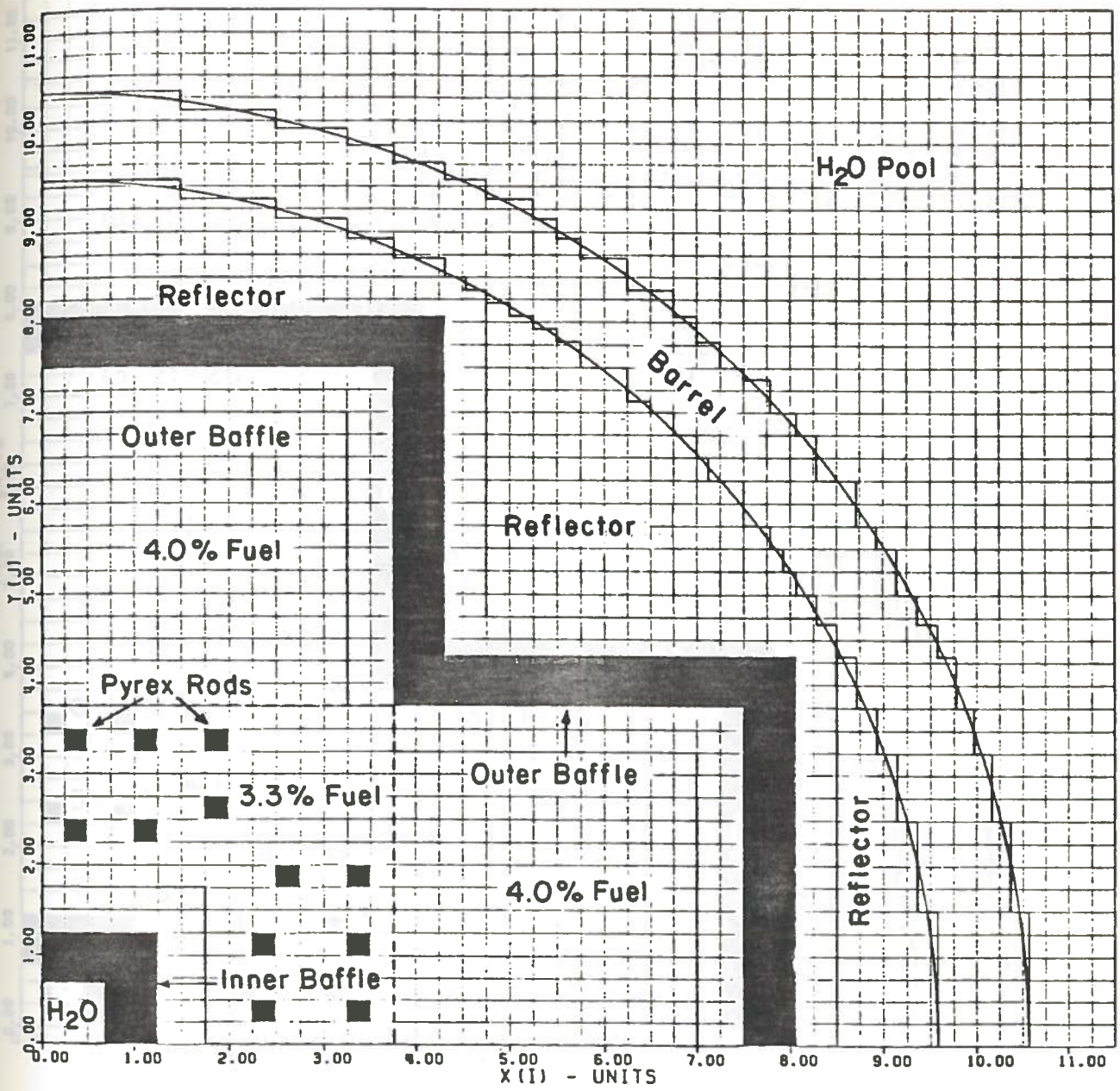

Fig. V-1. 1/4 Core of the VENUS 2-D Rectangular Model (Scale: 1 unit = 4 pin pitches = 5.04 cm).

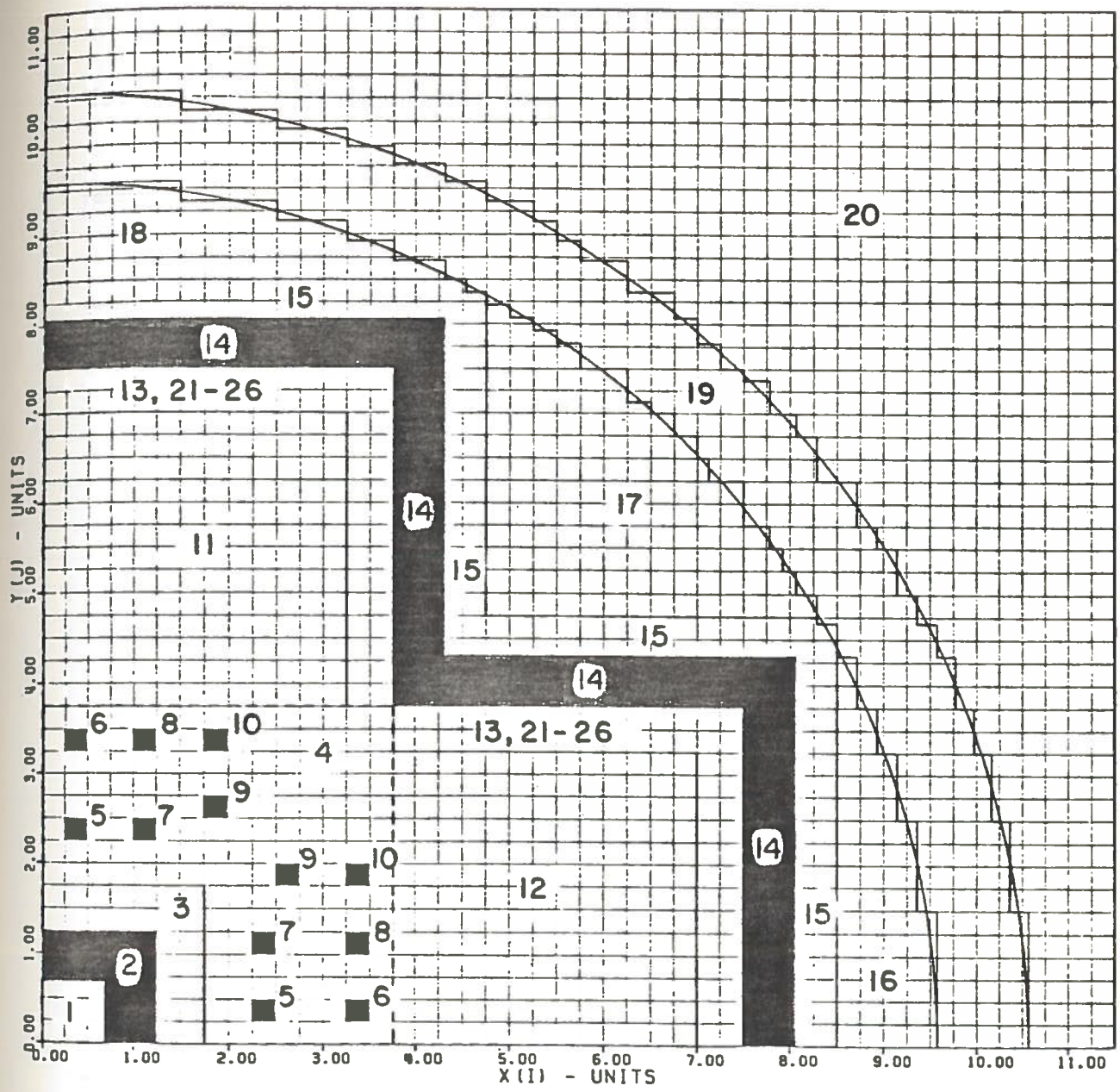

Fig. V-2. Zones used in the VENUS 2-D Eigenvalue Calculation (Scale: 1 unit = 4 pin pitches = 5.04 cm).

Table V-1. Definition of the Zones used in the VENUS 2-D Eigenvalue Calculation

Zone	Description	Composition
1	Water Hole	H_2O
2	Inner Baffle	SS-304
3	Inner 3.3% Fuel	3.3% Fuel
4	Outer 3.3% Fuel	3.3% Fuel + Pyrex
5-10	Pyrex	Pyrex
11-12	Inner 4.0% Fuel	4.0% Fuel
13	Outer 4.0% Fuel	4.0% Fuel
21-26	Outer 4.0 Fuel	4.0% Fuel
14	Outer Baffle	SS-304
15	Inner Reflector	H_2O
16-18	Outer Reflector	H_2O
19	Barrel	SS-304
20	Water Pool	H_2O

Table V-2. Atom Densities of the Mixtures used in the VENUS 2-D Calculations

Mixture	Nuclide	N ($\frac{\text{atoms}}{\text{barn-cm}}$)
H_2O	H	6.68652E-02
	O	3.34326E-02
SS-304 Baffle	Mn	1.18770E-03
	Cr	1.49840E-02
	Ni	7.06890E-03
	Fe	6.19945E-02
3.3% Fuel + Zircaloy Cladding + H_2O	U-234	2.22330E-06
	U-235	2.54050E-04
	U-236	1.22780E-06
	U-238	7.33343E-03
	Sn	4.78945E-05
	Zr	4.33881E-03
	H	3.70110E-02
	O	3.36790E-02
4.0% Fuel + SS-304 Cladding + H_2O	U-234	2.83120E-06
	U-235	3.65740E-04
	U-236	2.08270E-06
	U-238	8.61280E-03
	Mn	7.88830E-05
	Cr	1.18235E-03
	Ni	5.73925E-04
	Fe	4.21310E-03
	H	3.52260E-02
	O	3.55680E-02
Pyrex + SS-304 Cladding + H_2O	Si	3.91030E-03
	B-10	2.48980E-04
	B-11	1.01010E-03
	Al	1.29690E-04
	Na	3.32105E-04
	K	7.17700E-05
	Mn	2.71684E-05
	Cr	6.07112E-04
	Ni	2.77610E-04
	Fe	2.17809E-03
	H	3.52260E-02
	O	2.77215E-02

The interval boundaries are as depicted in Table V-3. Leakage in the axial direction was treated with a buckling approximation (DB^2 losses), using a buckling value of $B^2 = 24 \times 10^{-4}\ cm^{-2}$.

Using the appropriate diffusion coefficient values, the DB^2 values were determined and tabulated in Table V-4. See Appendix C for the method used to compute the diffusion coefficients. An ENDF/B-V[13] (as opposed to the ENDF/B-IV) based fission spectrum of Table V-5 was used in the 2-D calculation for better accuracy. Other necessary input arrays were determined, and entered into DOT IV. A flow chart of the DOT IV input and output scheme is shown in Fig. V-3.

The eigenvalue was calculated to be $k_{eff} = 0.996$, which is quite reasonable. On the basis of the 10 group fluxes obtained from the eigenvalue calculation, the space dependent total fission rate (for both U-235 and U-238) at each point within the core of the VENUS model was computed. In addition, activities for the U-235 fission rate in steel were calculated. Fission chamber activities for specified detector locations were computed,using the interpolation method of Taylor polynominal.

In order to compare the calculated fission rate values with the experimental measurements from Mol, it became necessary that the results be normalized consistently.

Table V-3. Mesh Intervals used in the 2-D Eigenvalue Calculation

Interval Boundary #	Radius (cm)	Midpoint (cm)	Delta R (cm)
1	0.0	3.15000E-01	6.30000E-01
2	6.30000E-01	9.44999E-01	6.30000E-01
3	1.26000E+01	1.41750E+00	3.15000E-01
4	1.57500E+00	1.73250E+00	3.15000E-01
5	1.89000E+00	2.04750E+00	3.15000E-01
6	2.20500E+00	2.36250E+00	3.15001E-01
7	2.52000E+00	2.75050E+00	4.61000E-01
8	2.98100E+00	3.21150E+00	4.61000E-01
9	3.44200E+00	3.64175E+00	3.99499E-01
10	3.84150E+00	4.04125E+00	3.99500E-01
11	4.24100E+00	4.44075E+00	3.99500E-01
12	4.64050E+00	4.84025E+00	3.99500E-01
13	5.04000E+00	5.19750E+00	3.15000E-01
14	5.35500E+00	5.51250E+00	3.15000E-01
15	5.67000E+00	5.82750E+00	3.15000E-01
16	5.98500E+00	6.14250E+00	3.15001E-01
17	6.30000E+00	6.61500E+00	6.30000E-01
18	6.93000E+00	7.24500E+00	6.30000E-01
19	7.56000E+00	7.87500E+00	6.30000E-01
20	8.19000E+00	8.50500E+00	6.30000E-01
21	8.82000E+00	8.97750E+00	3.15000E-01
22	9.13500E+00	9.29250E+00	3.15000E-01
23	9.45000E+00	9.60750E+00	3.15000E-01
24	9.76500E+00	9.92250E+00	3.15001E-01
25	1.00800E+01	1.07100E+01	1.26000E+00
26	1.13400E+01	1.14975E+01	3.15000E-01
27	1.16550E+01	1.18125E+01	3.15000E-01
28	1.19700E+01	1.21275E+01	3.15000E-01
29	1.22850E+01	1.24425E+01	3.15001E-00
30	1.26000E+01	1.27575E+01	3.15000E-01
31	1.29150E+01	1.30725E+01	3.15001E-01
32	1.32300E+01	1.33875E+01	3.15000E-01
33	1.35450E+01	1.37025E+01	3.15001E-01
34	1.38600E+01	1.44900E+01	1.26000E+00
35	1.51200E+01	1.57500E+01	1.26000E+00
36	1.63800E+01	1.65375E+01	3.14987E-01
37	1.66950E+01	1.68525E+01	3.15002E-01
38	1.70100E+01	1.71675E+01	3.15002E-01

Table V-3. (continued)

Interval Boundary #	Radius (cm)	Midpoint (cm)	Delta R (cm)
39	1.73250E+01	1.74825E+01	3.15002E-01
40	1.76400E+01	1.77975E+01	3.15002E-01
41	1.79550E+01	1.81125E+01	3.15002E-01
42	1.82700E+01	1.84275E+01	3.15002E-01
43	1.85850E+01	1.87425E+01	3.15002E-01
44	1.89000E+01	1.90786E+01	3.57239E-01
45	1.92572E+01	1.94359E+01	3.57254E-01
46	1.96145E+01	1.97931E+01	3.57254E-01
47	1.99717E+01	2.01504E+01	3.57254E-01
48	2.03290E+01	2.05076E+01	3.57239E-01
49	2.06862E+01	2.08649E+01	3.57254E-01
50	2.10435E+01	2.12221E+01	3.57254E-01
51	2.14007E+01	2.15794E+01	3.57254E-01
52	2.17580E+01	2.19398E+01	3.63663E-01
53	2.21217E+01	2.23035E+01	3.63663E-01
54	2.24853E+01	2.26671E+01	3.63663E-01
55	2.28490E+01	2.30308E+01	3.63663E-01
56	2.32126E+01	2.33945E+01	3.63663E-01
57	2.35763E+01	2.37581E+01	3.63678E-01
58	2.39400E+01	2.45700E+01	1.25999E+00
59	2.52000E+01	2.58300E+01	1.25999E+00
60	2.64600E+01	2.70900E+01	1.25999E+00
61	2.77200E+01	2.83500E+01	1.26001E+00
62	2.89800E+01	2.96100E+01	1.25999E+00
63	3.02400E+01	3.08700E+01	1.25999E+00
64	3.15000E+01	3.21300E+01	1.26001E+00
65	3.27600E+01	3.33900E+01	1.25999E+00
66	3.40200E+01	3.46500E+01	1.26001E+00
67	3.52800E+01	3.54900E+01	4.19998E-01
68	3.57000E+01	3.59100E+01	4.19998E-01
69	3.61200E+01	3.63300E+01	4.19998E-01
70	3.65400E+01	3.66660E+01	2.51999E-01
71	3.67920E+01	3.69180E+01	2.51999E-01
72	3.70440E+01	3.71700E+01	2.51999E+01
73	3.72960E+01	3.74220E+01	2.51999E-01
74	3.75480E+01	3.76740E+01	2.52014E-01
75	3.78000E+01	3.79786E+01	3.57239E-01
76	3.81572E+01	3.83358E+01	3.57254E-01
77	3.85145E+01	3.86931E+01	3.57254E-01
78	3.88717E+01	3.90504E+01	3.57254E-01
79	3.92290E+01	3.94076E+01	3.57239E-01

Table V-3. (continued)

Interval Boundary #	Radius (cm)	Midpoint (cm)	Delta R (cm)
80	3.95862E+01	3.97648E+01	3.57254E-01
81	3.99435E+01	4.01221E+01	3.57254E-01
82	4.03007E+01	4.04794E+01	3.57254E-01
83	4.06580E+01	4.08398E+01	3.63663E-01
84	4.10217E+01	4.12035E+01	3.63663E-01
85	4.13853E+01	4.15671E+01	3.63663E-01
86	4.17490E+01	4.19308E+01	3.63663E-01
87	4.21126E+01	4.22945E+01	3.63663E-01
88	4.24763E+01	4.26581E+01	3.63678E-01
89	4.28400E+01	4.33818E+01	1.08360E+00
90	4.39236E+01	4.44654E+01	1.08360E+00
91	4.50072E+01	4.55490E+01	1.08360E+00
92	4.60908E+01	4.66326E+01	1.08360E+00
93	4.71744E+01	4.77162E+01	1.08360E+00
94	4.82580E+01	4.87557E+01	9.95392E-01
95	4.92534E+01	4.97511E+01	9.95392E-01
96	5.02488E+01	5.07465E+01	9.95407E-01
97	5.12442E+01	5.17419E+01	9.95392E-01
98	5.22396E+01	5.27373E+01	9.95407E-01
99	5.32350E+01	5.37075E+01	9.44992E-01
100	5.41800E+01	5.46525E+01	9.44992E-01
101	5.51250E+01	5.55975E+01	9.45007E-01
102	5.60700E+01	5.65425E+01	9.44992E-01
103	5.70150E+01	5.74875E+01	9.45007E-01
104	5.79600E+01		

Note: I-Mesh Intervals ≡ J-Mesh Intervals

Table V-4. 10 Group Axial Leakage Approximation

	$[DB^2]_{z,g}$ (cm^{-1})			
	Zones			
Group	1,15-18,20 (H_2O)	3-10 (3.3% Fuel + Pyrex)	11-13,21-26 (4.0% Fuel)	2,14,19 (SS-304)
1	5.3842E-03	5.5355E-03	5.2252E-03	4.1736E-03
2	2.5306E-03	2.7914E-03	2.7841E-03	4.1258E-03
3	1.4246E-03	1.6644E-03	1.6723E-03	2.3227E-03
4	1.0034E-03	1.2249E-03	1.1874E-03	1.1737E-03
5	9.2890E-04	1.1802E-03	1.1354E-03	9.3560E-04
6	9.3100E-04	1.1878E-03	1.1053E-03	7.6870E-04
7	9.2420E-04	1.1525E-03	1.0787E-03	8.9610E-04
8	8.8470E-04	11363E-03	1.0689E-03	8.7890E-04
9	8.0010E-04	1.1063E-03	1.0456E-03	8.5200E-04
10	3.1770E-04	5.6010E-04	5.4410E-04	7.5860E-04

Table V-5. Fission Spectrum used in the 2-D VENUS Calculation

Group	Fission Spectrum*
1	4.43542E-01
2	5.01062E-01
3	5.31616E-02
4	2.14101E-03
5	1.00746E-04
6	5.37419E-06
7	2.53420E-07
8	1.27239E-08
9	8.80453E-10
10	2.29249E-10

* These values are based on ENDF/B-V data.

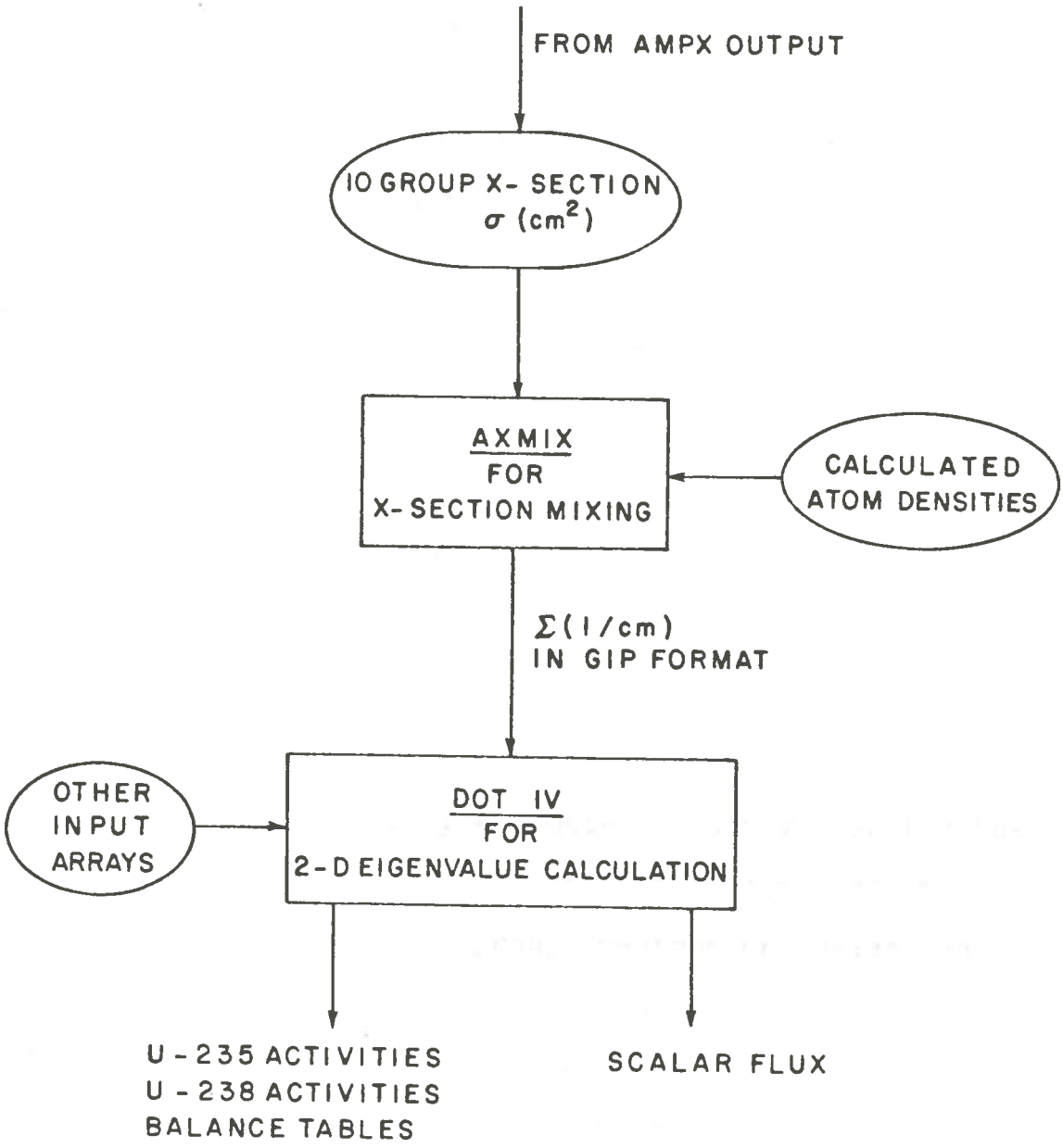

Fig. V-3. Flow Chart of DOT IV Input and Output.

The normalization process was effected by first calculating the total fission rate (for both U-235 and U-238), integrated over the entire reactor core. This value was then divided by the total number of cells in the core to determine the average fission rate per cell. Finally, the calculated space dependent fission rate at each point in the reactor core was divided by the average fission rate per cell to obtain the relative power distribution. The normalization of the calculated and measured fission chamber results was different than for the core power distribution. In this case, the results were both normalized to 1.0 at a specified position in the inner baffle.

V.2. Fixed Source Calculation

In order to accurately estimate the activities for the Np-237 fission chamber results, it became necessary that a 56 group (instead of the 10 group) neutron cross-section be used. The fission cross section for Np-237 has a high energy threshold, and the 10 group structure does not adequately represent the high energy range. Thus, a new transport calculation which used the 56 group ELXSIR[14] cross-section library, and a fixed fission source was performed. The fixed source used in the calculations corresponded to the VENUS core fission source obtained from the 10 group eigenvalue calculation. The same mesh was

used in the 56 group results. However, only one boundary zone was used to represent the outer 4.0% fuel region (as opposed to 7 zones in the 10 group calculation), because the effect of thermal neutrons is insignificant in this calculation. The flow chart of the 56 group DOT IV calculation is shown in Fig. V-4.

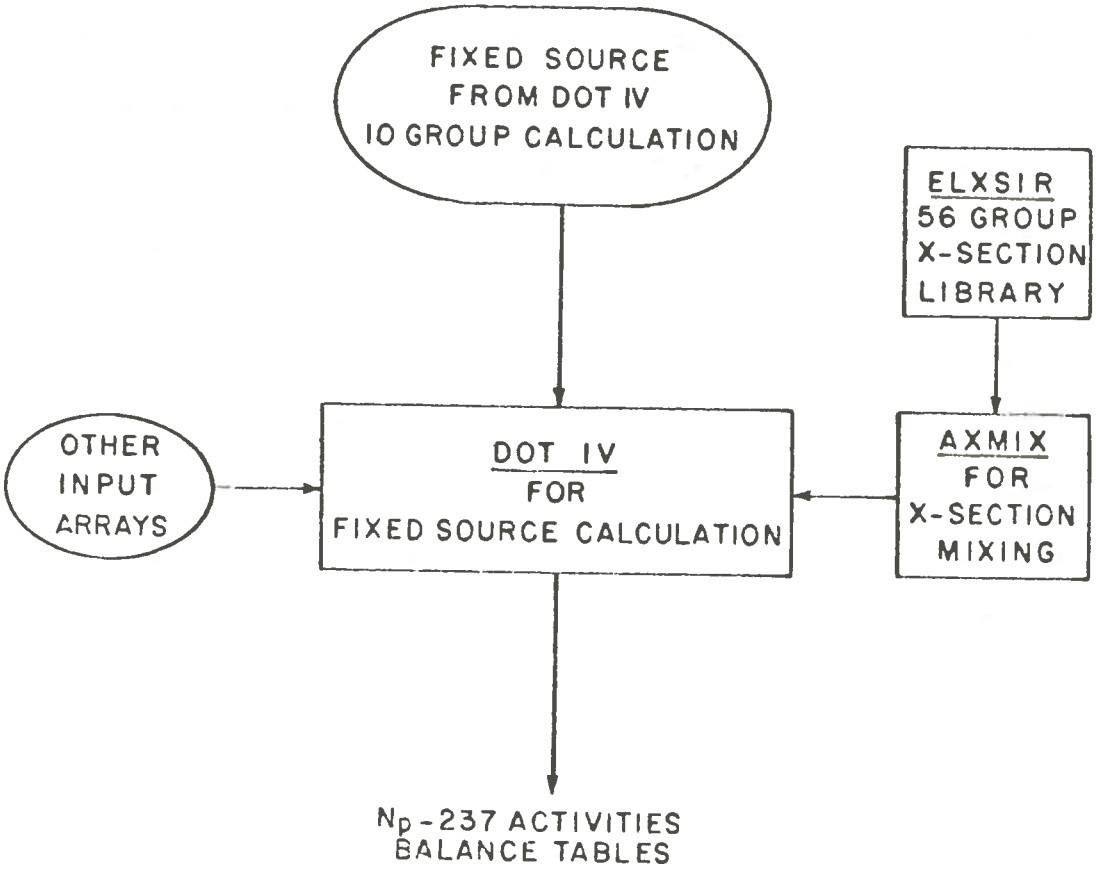

Fig. V-4. Flow Chart of the 56 Group DOT IV Calculation.

Chapter VI

RESULTS

VI.1 One-Dimensional Calculations

While performing the 218 group one-dimensional transport calculations, it was observed that the thermal neutron spectrum hardens around the periphery of the core-baffle* interface. This behavior has an effect on the collapsed thermal cross-section values used in the two-dimensional calculations. It was realized from the on-set that a transition would occur in the region near the baffle from an asympotic core spectrum to one representative of a thermal spectrum in iron. Prior to the present calculations, a transition zone of 2.52 cm with weighted cross-section were used. However, it was later realized that a single transition zone of 2.52 cm is too coarse, due to the rapid changes in the thermal spectrum within the last 2 cm of the core boundary. It became necessary that more zones be used in the core-baffle region to account properly for the thermal spectrum changes. As a result, a total of seven zones were used for the one-dimensional calculations to obtain a

---

* This discussion is confined to the outer baffle-core region, since this is the area that contributes most to RPV fluence.

separately weighted set of collapsed cross-sections at approximately every one-quarter centimeter in the core-baffle region of 2.52 cm. The effect of this zone-weighting procedure on the collapsed U-235 thermal fission cross-section is shown in Table VI-1. Notice the significant variation of the cross-sections in the core-baffle region of 2.52 cm. Also in the two-dimensional calculation, seven zones with different cross-section weightings were used for the core-baffle region.

VI.2 Two-Dimensional Calculations

The effective multiplication factor for the two-dimensional X-Y calculations was determined to be $k_{eff} = 0.996$. This value was underpredicted by about one half of one percent. The low value of k_{eff} is consistent with other LWR lattice studies which show that the ENDF/B-IV cross-sections tend to underestimate the eigenvalue due to excessive U-238 capture estimates.

A set of 10 group fluxes was obtained from the eigenvalue calculation. Three-dimensional plots of the thermal flux (i.e. group 10 with $E < 0.650$ eV), and the fast flux of group 1 (with $E > 1.850$ MeV), as a function of position for the VENUS model are shown in Figs. VI-1 and VI-2 respectively. The plot of Fig. VI-1 shows that the thermal flux has its highest peak at the core center in the water hole. This is due to the fact that a lot of the fission neutrons are thermalized in the water hole.

Table VI-1. Variation of U-235 Thermal Fission Cross-Section*

Distance from Outer Baffle (cm)	Description	U-235 Group 10/10 Fission Cross-Section (barns)
0.252	Outer 4.0% Fuel	250.35
0.504	Outer 4.0% Fuel	255.79
0.756	Outer 4.0% Fuel	259.64
1.008	Outer 4.0% Fuel	262.40
1.260	Outer 4.0% Fuel	264.55
1.512	Outer 4.0% Fuel	266.28
2.520	Outer 4.0% Fuel	269.41
2.52-18.90	Inner 4.0% Fuel	278.80

* These are collapsed values and are applicable to the 4.0% fuel region only.

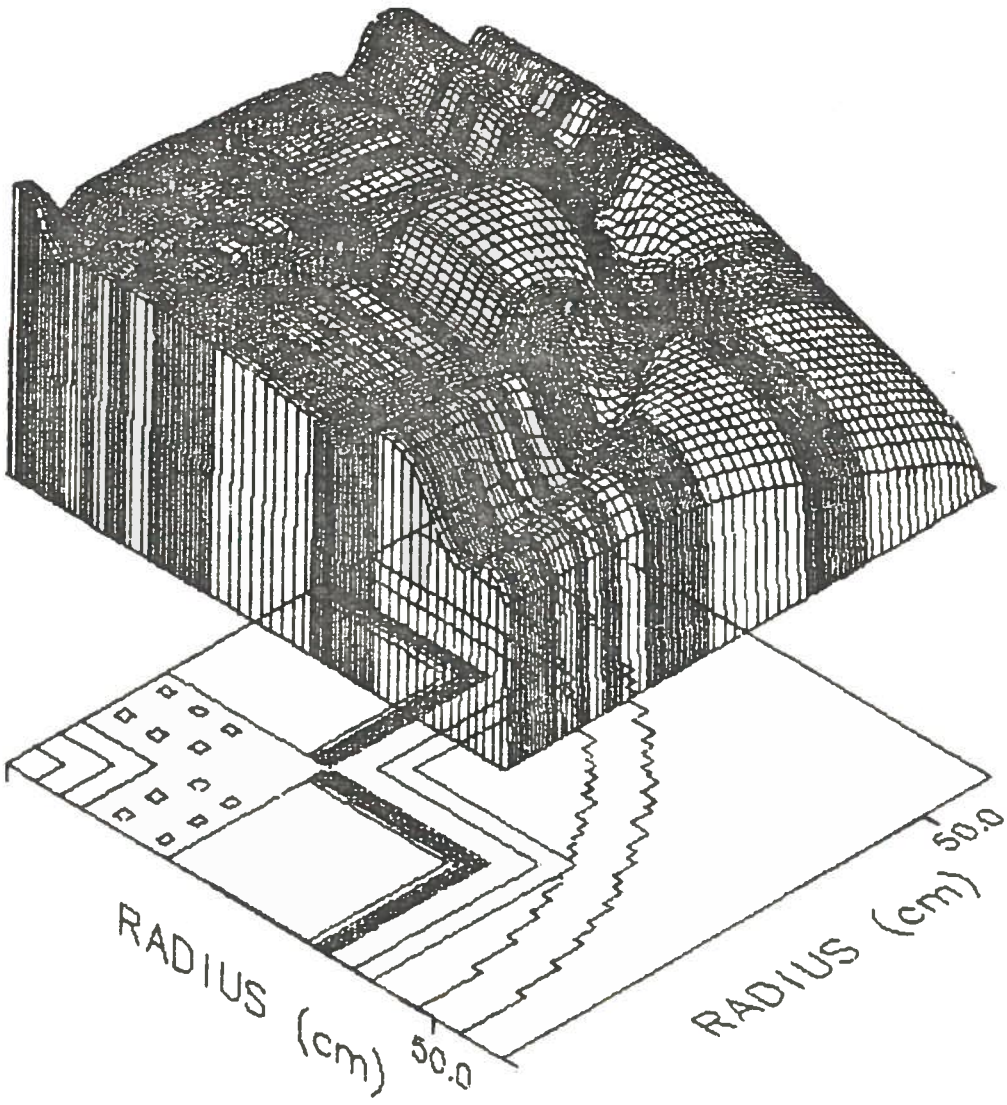

Fig. VI-1. Thermal Flux of Group 10 for the VENUS Model.

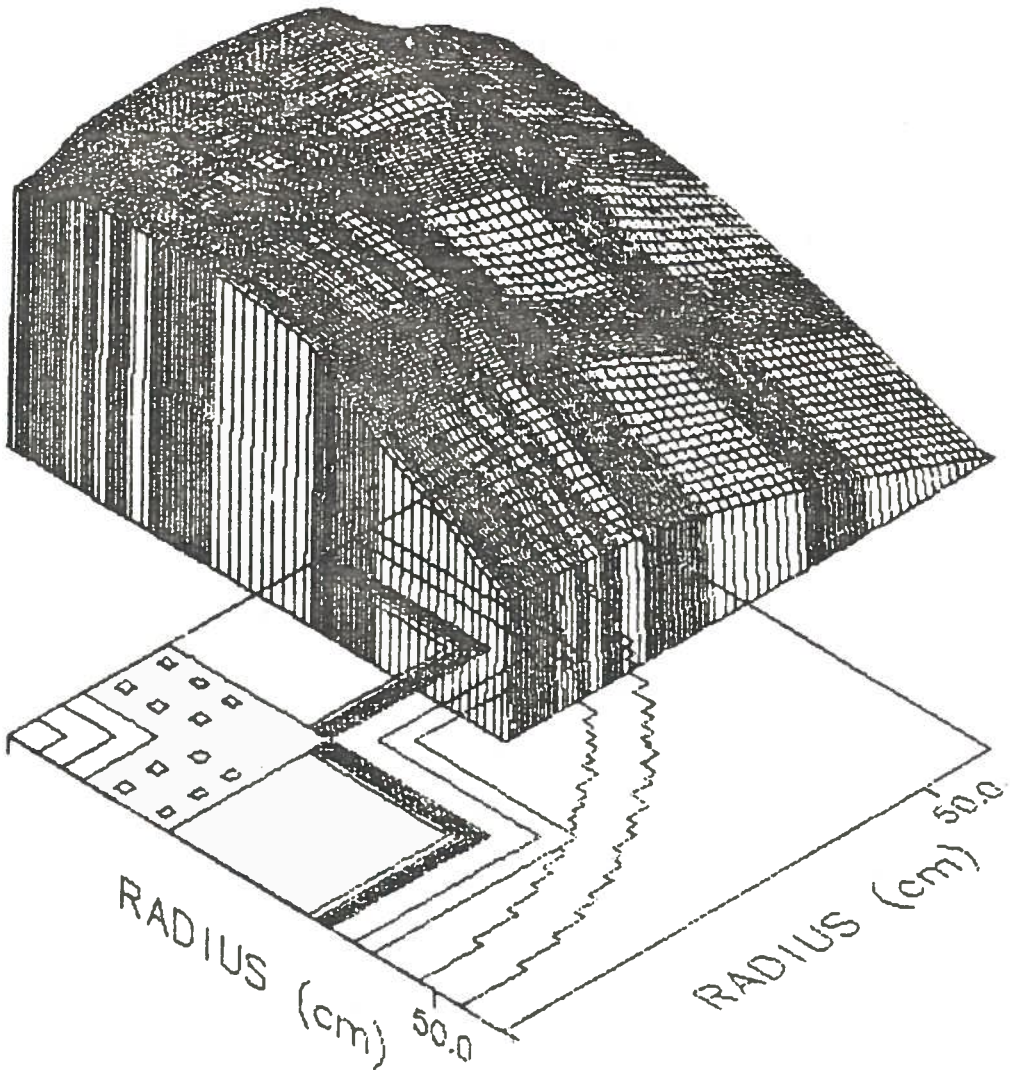

Fig. VI-2. Fast Flux of Group 1 for the VENUS Model.

Other peaks can be observed in the water reflector region, and the water pool. Notice the depression of thermal flux in the steel baffles and barrel. The biggest flux depression is in the steel barrel, and this is because the flux sees more iron in the barrel, relative to the baffles. On the other hand, the plot of Fig. VI-2 indicates that the fast flux peaks around the fuel cells area, and there is no depression in iron. Notice the flattening of the fast flux peak, which is due to the pyrex cells. It can also be seen that the number of fast neutrons decreases towards the core edges, and it reaches a minimum in the water pool.

On the basis of the 10 group fluxes, the total space dependent fission rate throughout the core was calculated, accounting for both U-235 and U-238 fissions. The U-235 is the fission rate due to thermal and epithermal neutrons, and the U-238 is the fission rate due to fast neutrons. The fission distribution was normalized to obtain a relative pin-to-pin power distribution as shown in Fig. VI-3. These calculations used the detailed spatially weighted cross-sections near the core-baffle interface.

Fission chamber results for the 10 group X-Y calculation (i.e. U-235 activity) and the 56 group calculation (i.e. Np-237 activity) were obtained at selected locations in the steel baffle and in the steel barrel of the VENUS core. The U-235 activity is for low energy neutrons; and the Np-237 activity, which has a threshold of about 100 KeV,

Unit: Total fission/sec./cell

NORMALIZATION

Core average fission rate =
1 fiss./sec./cell

Total 1/8 Core = 319 fiss./sec.

Total Core = 2552 fiss./sec.

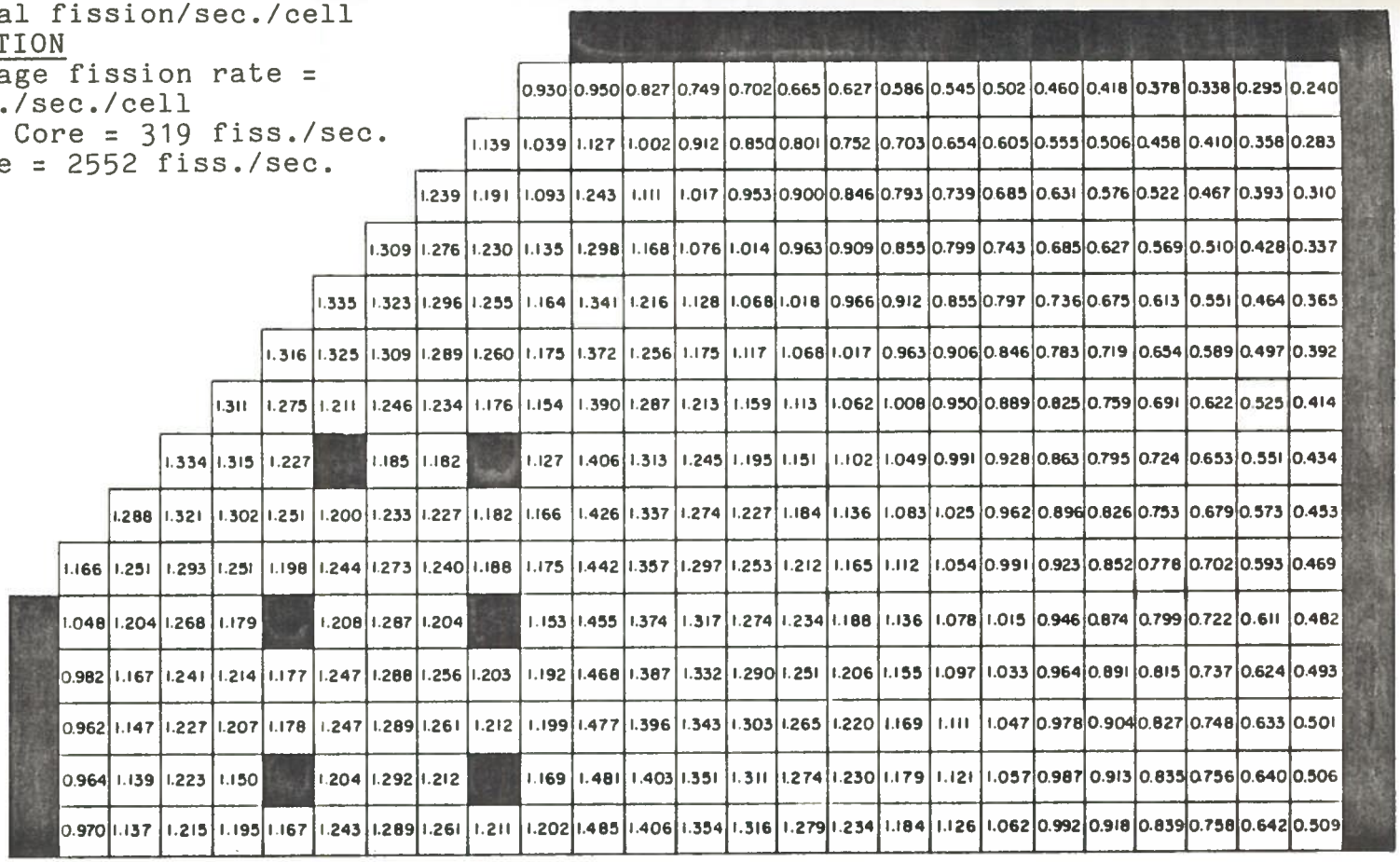

Fig. VI-3. Calculated Radial Power Distribution for 1/8 of the VENUS Core.

is for high energy neutrons. The locations are shown in Fig. VI-4. The fission rate results and the corresponding normalized values are given in Table VI-2.

VI-3 Experimental Measurements[15]

By using gamma scans of various fuel pins removed from the core, Mol was able to deduce the relative fission rates in the VENUS Core. Fig. VI-5 shows the normalized values of the experimentally measured power distribution. Notice that some of the values were obtained by interpolation.

The U-235 and Np-237 fission chamber measurements for locations shown in Fig. VI-4 are given in Table VI-3.

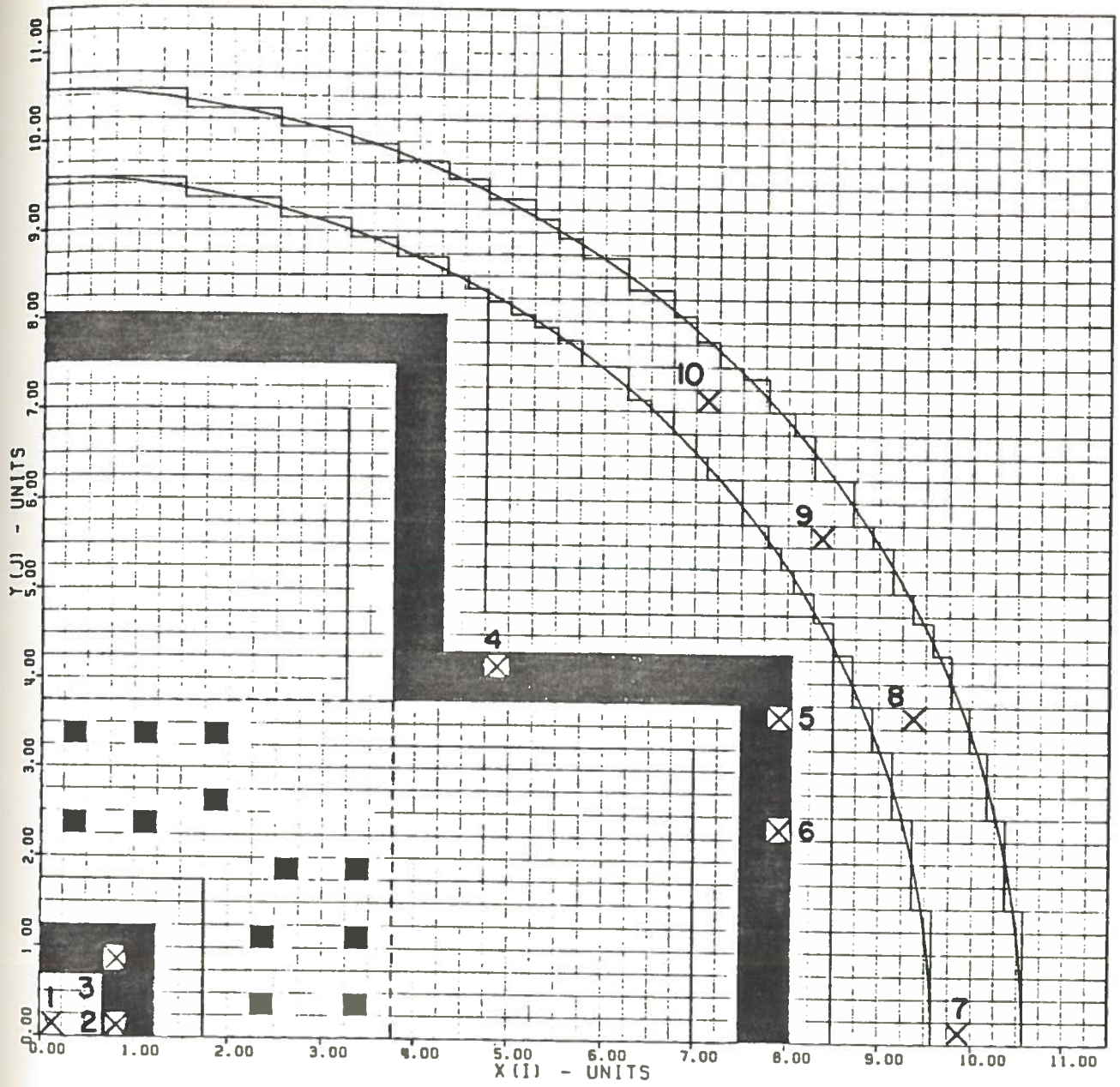

Fig. VI-4. Fission Chamber Locations in the VENUS Model (Scale: 1 unit = 4 pin pitches = 5.04 cm).

Table VI-2. Results of Fission Chamber Calculations

#	Position†	X(I) cm	Y(J) cm	U-235 Fission Rate		Np-237 Fission Rate	
				Calculated Value	Normalized* Value	Calculated Value	Normalized* Value
1	WH(45°)	0.63	0.63	11.1800	7.2597	6.695E-03	0.6205
2	IB(8.13°)	4.41	0.63	1.5400	1.0	1.079E-02	1.0
3	IB(45°)	4.41	4.41	0.9660	0.6273	1.275E-02	1.1816
4	OB(40.24°)	24.57	20.79	0.7540	0.4896	6.380E-03	1.5913
5	OB(24.72°)	39.69	18.27	0.2730	0.1773	1.985E-03	0.1840
6	OB(16.78°)	39.69	11.97	0.4010	0.2604	3.315E-03	0.3072
7	B(0.725°)	49.77	0.63	0.1560	0.1013	5.030E-04	0.0466
8	B(21.14°)	47.25	18.25	0.0865	0.0562	4.600E-04	0.0426
9	B(33.9°)	42.21	28.35	0.0586	0.0380	3.250E-04	0.0301
10	B(45°)	35.91	35.91	0.0538	0.0349	2.2557E-04	0.0209

* Normalized to 1.0 at IB(8.13°) position.
† WH = Water Hole, IB = Inner Baffle, OB = Outer Baffle, B = Barrel.

Note: Underlined values are experimental data. Other values are interpolated.
Unit: Total fission/sec/cell

NORMALIZATION

Core average fission rate = 1 fiss./sec./cell

Total 1/8 Core = 319 fiss./sec.

Total Core = 2552 fiss./sec.

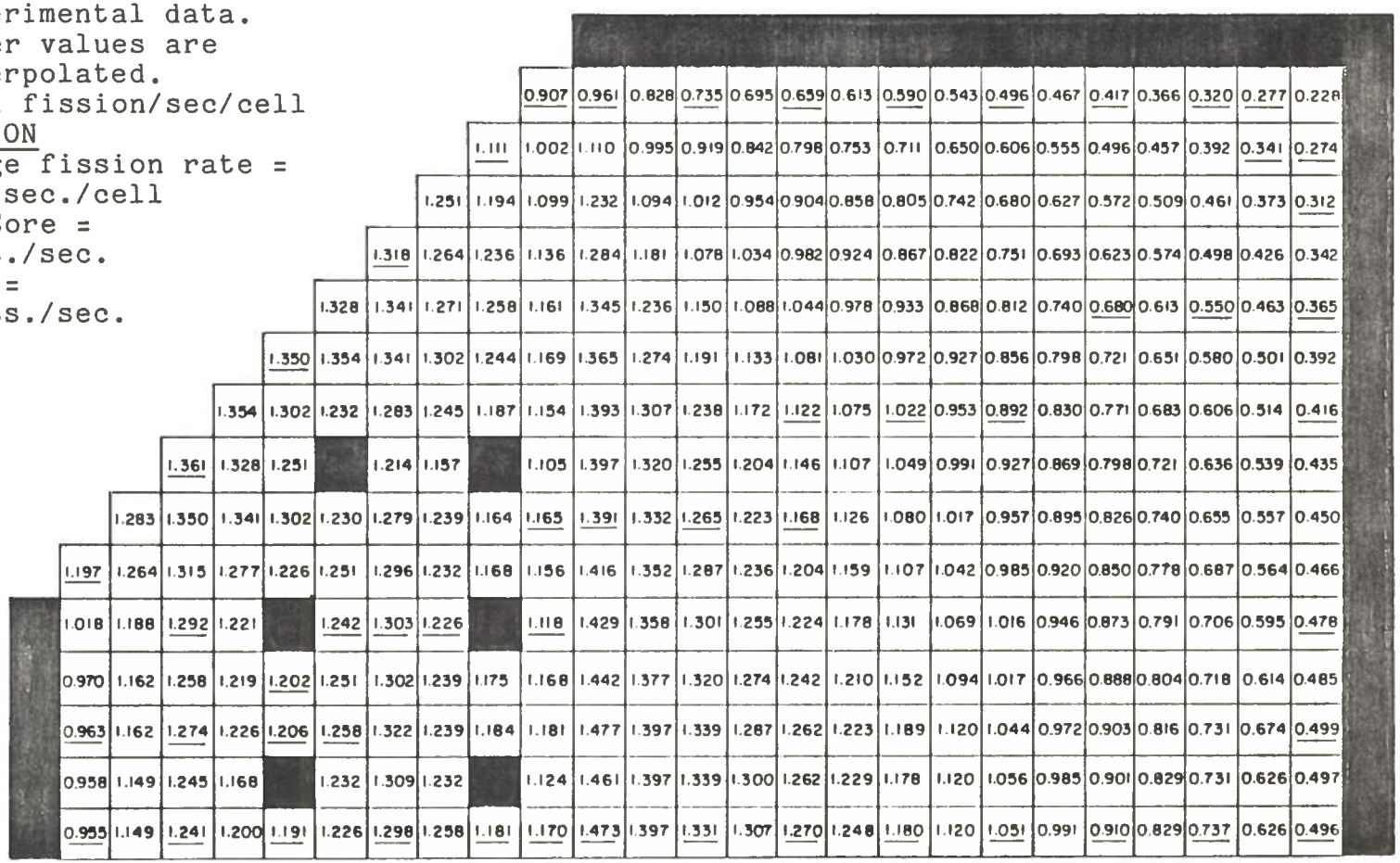

Fig. VI-5. Measured Radial Power Distribution of the VENUS Core.

Table VI-3. Results of Fission Chamber Experimental Measurements

#	Position†	X(I) cm	Y(J) cm	U-235 Fission Rate		Np-237 Fission Rate	
				Measured Value	Normalized* Value	Measured Value	Normalized* Value
1	WH(45°)	0.63	0.63	-	-	1.550E+09	0.6568
2	IB(8.13°)	4.41	0.63	4.960E-13	1.0	2.360E+09	1.0
3	IB(45°)	4.41	4.41	-	-	2.800E+09	1.1864
4	OB(40.24°)	24.57	20.79	2.520E-13	0.5081	1.410E+09	0.5974
5	OB(24.72°)	39.69	18.27	-	-	4.240E+08	0.1797
6	OB(16.78°)	39.69	11.97	1.290E-13	0.2601	7.380E+09	0.3127
7	B(0.725°)	49.77	0.63	-	-	1.180E+08	0.0500
8	B(21.14°)	47.25	18.25	2.630E-14	0.0530	1.090E+08	0.0462
9	B(33.9°)	42.21	28.35	-	-	7.330E+07	0.0310
10	B(45°)	35.91	35.91	1.460E-14	0.0294	5.510E+07	0.0233

* Normalized to 1.0 at IB(8.13°) position.
† WH = Water Hole, IB = Inner Baffle, OB = Outer Baffle, B = Barrel.

Chapter VII

COMPARISON OF CALCULATION TO MEASUREMENTS AND DISCUSSION OF RESULTS

VII.1 Comparison of Calculational and Experimental Measurements

Relative Power Distribution

A comparison of the calculated and measured relative power distribution of the VENUS model is shown in Fig. VII-1. The average agreement between calculation and experiment is within 3% error, with an uncertainty of about 1.5% in the measurements. The worst agreement has an error of 6.5%, and it occurs in a cell near the baffle corner. Disagreements of up to 3% can also be found at locations near the pyrex rods. The error introduced into the computed RPV fluence by these source discrepancies should be on the order of 5% or less. Agreement could be improved, perhaps, by adding more zones in the core-baffle interface region.

Fission Chamber Responses

The ratio of the fission chamber response calculations to experimental measurements are given in Table VII-1. The corresponding fission chamber locations can be found in Fig. VI-4. Both the calculated and measured values are normalized so that the U-235 and Np-237 fission rate at

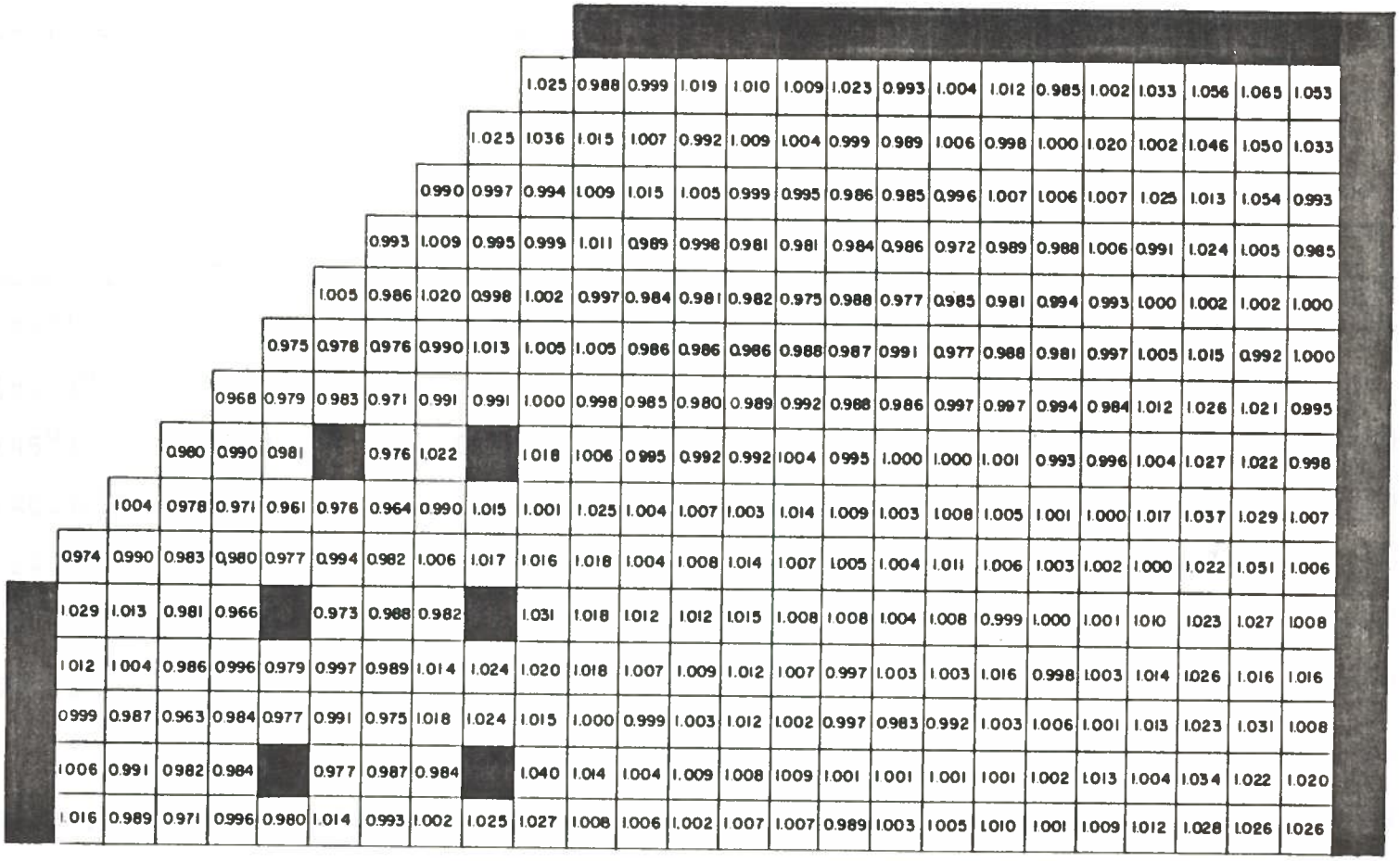

Fig. VII-1. Comparison of Calculated and Measured Relative Power Distribution.

Table VII-1. Comparison of Fission Chamber Calculations with Experiment

#	Position†	X(I) cm	Y(J) cm	U-235			Np-237		
				Calc.	Expt.	C/E	Calc.	Expt.	C/E
1	WH(45°)	0.63	0.63	7.2597	-	-	0.6205	0.6568	0.9447
2	IB(8.13°)	4.41	0.63	1.0	1.0	1.0	1.0	1.0	1.0
3	IB(45°)	4.41	4.41	0.6273	-	-	1.1816	1.1864	0.9959
4	OB(40.24°)	24.57	20.79	0.4896	0.5081	0.9636	0.5913	0.5974	0.9898
5	OB(24.72°)	39.69	18.27	0.1773	-	-	0.1840	0.1797	1.0239
6	OB(16.78°)	39.69	11.97	0.2604	0.2601	1.0011	0.3072	0.3127	0.9824
7	B(0.725°)	49.77	0.63	0.1013	-	-	0.0466	0.0500	0.9320
8	B(21.14°)	47.25	18.25	0.0562	0.0530	1.0604	0.0426	0.0462	0.9221
9	B(33.9°)	42.21	28.35	0.0380	-	-	0.0301	0.0310	0.9710
10	B(45°)	35.91	35.91	0.0349	0.0294	1.1871	0.0209	0.0233	0.8970

† WH = Water Hole, IB = Inner Baffle, OB = Outer Baffle, B = Barrel.

point 2 in the inner baffle is equal to unity. It can be seen that the relative C/E values in the baffles are very close to unity, indicating good agreement. The worst agreement is in the barrel, and this can be attributed to the fact that a rectangular approximation was used for the circular barrel. Nevertheless, the average agreement between calculation and experiment is good, considering the fact that the U-235 and Np-237 dosimeters were located in the ex-core areas, for which the R-θ calculational model is best suited.

VII.2 Discussion of Results

The Analysis of the fission rate calculation shows that the fission source peaks around the 3.3% and 4.0% fuel boundary region, with the 4.0% fuel contributing the most (about 64%) to the total fission rate, and the 3.3% fuel contributing the highest average peak values. Results also indicate that the fission source approaches a minimum at the core-outer baffle interface, with the ultimate minimum at the steel baffle corner. If there were no outer baffle at the core boundary, the neutrons that thermalize in the water reflector would have contributed significantly to the fission source at the fuel-reflector region to establish a local maximum of neutrons. The fact that we have a local minimum suggests that the steel baffle is consuming the neutrons which thermalize in the water reflector before they

can re-enter the core. The result is that the RPV fluence is greatly reduced by the presence of the outer baffle.

While the fission rate in the last row of the fuel cells approaches a minimum at the outer baffle corner, the fission rate of the fuel cells along the inner baffle decreases to a minimum, and then increases to a maximum at the corner. This behavior is a duplication of the thermal flux distributin in the region and it is probably due to a combination of the slowing down neutrons and the thermal neutrons from the water hole. It should be mentioned that the core neutron source distribution measurements from Mol does not reflect this phenomenon, probably because most of the measurements in the region were obtained by interpolation.

It can also be observed that the flux around the pyrex region is depressed, resulting in an appreciable flattening of the core power distribution. The result is that the power distribution spreads to the core edges in order to facilitate accurate ex-core measurements.

The normalized fission chamber results show that the calculated U-235 values are slightly higher than the normalized measured values, while the calculated Np-237 values are slightly lower than the normalized measured values. Essentially, the C/E values for U-235 are slightly greater than unity while we have low C/E values for Np-237.

It can also be seen that the Np-237 disagreement increases with more iron penetration, paticularly in the steel barrel. The low C/E values for Np-237 is probably due to the ENDF/B-IV iron inelastic cross-sections which are thought to be too large, thereby resulting in an overprediction of attenuation of high energy neutrons through the baffles and barrel.

The U-235 fission rate results obtained from the 56 group calculation was compared to the measured U-235 fission chamber responses, and it was found that the errors are of higher magnitude, relative to the errors from the U-235 fission chamber results of the 10 group calculation. This is because the ELXSIR 56 group cross-section library was derived from the VITAMIN-C cross-section library, which has a "generic" thermal group cross-section, and therefore does not adequately represent the thermal spectrum in the various zones of the VENUS configuration.

Measurements in the inner baffle can be related to measurements in the outer baffle since both baffles are bounded by water which thermalize the fission neutrons. In essence, the water hole provides a reference field for checking the validity of the techniques used for the study of the neutron propagation across the baffle and outside the core. In addition, the water hole shifts the power peak

towards larger radii, thereby improving the core power distribution.

The fact that the overall calculation is in good agreement with experimental measurements establishes that uncertainties in the core source calculation are tolerable in the computation of the RPV fluence.

Chapter VIII

CONCLUSIONS AND RECOMMENDATIONS

VIII.1 Conclusions

Few group cross-sections were generated and shown to give better agreement with experiment for thermal responses like U-235 fission, than the ELXSIR (or VITAMIN-C) cross-section library.

An important discovery of this thesis is that the thermal flux changes rapidly as a function of position in the outer baffle-core interface region, which is the most important region for contributing to RPV fluence. It was discovered that the neutron source in the core-baffle region can be accurately calculated by using several separately weighted cross-sections at the appropriate points in the region. An increased number of separately weighted cross-sections correponds to a greater degree of accuracy; however, this significantly increases the calculational complexity and may not be practical for analysis of power reactors. A total of seven separately weighted cross-sections were used in the core-baffle interface region of the VENUS model.

Comparison of calculation with measured relative power distribution indicate that the shape of the neutron source

can be computed to an accuracy of within 6% error near the important core-baffle region, and an average agreement of about 3% error for the whole in-core area. Also, the compared values of the calculated and measured U-235 thermal neutron and Np-237 fast neutron fission rates in the ex-core region are in good agreement. The worst agreement is in the circular barrel, which was approximated in the X-Y model as a rectangular geometry. It is believed that a better accuracy for the ex-core calculation can be obtained with an R-θ model of the VENUS configuration.

In retrospect, all the goals outlined for this thesis have been achieved, particularly the ultimate goal of calculating the neutron source distribution within the VENUS core. In conclusion, the space dependent neutron fission rate in the VENUS core, particularly at the core periphery can be accurately calculated with discrete ordinates transport theory. A high degree of accuracy can be obtained by using a detailed set of space dependent cross-section weightings in the important outer baffle-core interface region.

VIII.2 Recommendations for Future Work

It is recommended that an R-θ model be used in the ex-core calculations, which is expected to include the surveillance dosimeter measurements and the RPV fluence calculation that is commonly used in assessing RPV embrit-

tlement. Mol has recently obtained neutron spectrum measurements with proton recoil spectrometers, and these measurements should be compared with the calculated 56 group spectrum.

In addition to the neutronic studies, the gamma flux distribution needs to be calculated, with a view of providing estimates of the gamma doses and heating rates at several locations, and the ratio of gamma dose rate to thermal neutron flux.

Finally, the VENUS benchmark can be extended to validate the two group diffusion theory, which is the standard core analysis method used by utilities. This will provide a true measure of the effectiveness of the diffusion theory method, relative to the discrete ordinates transport theory method.

REFERENCES

1. T. U. Marston et al., "A Report on the EPRI Pressurized Thermal Shock Program," Presented at the 10th Water Reactor Safety Research Information Meeting, Gaithersburg, Maryland, October 15, 1982.

2. R. D. Cheverton, "A Brief Account of the Effect of Overcooling Accidents on the Integrity of PWR Pressure Vessels," NUREG/CP-0029, Vol. II, March 1982.

3. R. Smock, "Thinking the Unthinkabble: NRC's Guidlines Aimed at Preventing Pressure Vessel Failure," Electric Light and Power, December 1982.

4. G. Minsart, "Design Study of the Core Loading for the VENUS PWR Pressure Vessel Benchmark Facility," CEN/SCK, Mol, Report 380/82-27, October 5, 1982.

5. L. Leenders, "Definition of Qualification of the Materials Used in the VENUS Configuration," Correspondence from CEN/SCK in Mol, Belgium to Oak Ridge National Laboratory, 1983.

6. W. E. Ford, III, C.C. Webster, and R.M. Westfall, "A 218 Group Neutron Cross-Section Library in the AMPX Master Interface Format for Criticality Safety Studies," ORNL/CSD/TM-4, July 1976.

7. L. W. Nordheim, "Theory of Resonance Absorption," Proceedings of Symposia in Applied Mathematics, Vol. XI, p. 58, G. Birkhoff and E. P. Wigner, Eds., American Mathematics Society, 1961.

8. R. M. Westfall, L. M. Petrie, N. M. Greene, and J. L. Lucius, "NITAWL-S: Scale System Module for performing Resonance Shielding and Working Library Production," NUREG/CR-0200, Vols. 1-3, ORNL/NUREG/CSD-2/R1, July 1982.

9. L. M. Petrie, N. M. Greene, J. L. Lucius, and J. E. White, "NITAWL: AMPX Module for Resonance Self-Shielding and Working Library Production," PSR-63/AMPX-II, November 1978.

10. L. M. Petrie and N. M. Greene, "XSDRNPM-S: A One-Dimensional Discretes Ordinates Code for Transport Analysis," NUREG/CR-0200, Vol. 2, Section F3, ORNL/NUREG/CSD-2/V3/R1.

11. N.M. Greene et al., "AMPX: A Modular System for Multigroup Cross-Section Generation and Manipulation," A Review of Multigroup Nuclear Cross-Section Processing Proceedings of a Seminar-Workshop, Oak Ridge, Tennessee, March 14-16, 1978.

12. W.A. Rhoades and R. L. Childs, "An Updated Version of the DOT IV One- and Two-Dimensional Neutron/Photon Transport Code," ORNL-5851, April 1982.

13. W. E. Ford, III et al., "CSRL-V: Processed ENDF/B-V 227-Neutron-Group and Pointwise Cross-Section Libraries for Criticality Safety, Reactor and Shielding Studies," NUREG/CR-2306, ORNL/CSD/TM-160, June 1982.

14. M. L. Williams, R. E. Maerker, W. E. Ford, III, and C.C. Webster, "The ELXSIR Cross-Section Library for LWR Pressure Vessel Irradiation Studies," Oak Ridge National Laboratory, July 1983.

15. A. Fabry et al., "Experimental Results," Correspondence from CEN/SCK in Mol, Belgium to Oak Ridge National Laboratory, 1983/84.

16. J. R. Lamarsh, "Introduction to Nuclear Reactor Theory, " Addison-Wesley Publishing Co., pp. 370-400, 1966.

17. A. F. Henry, "Nuclear Reactor Analysis," The MIT Press, pp. 66-80, 84-87, 200-253, 333-343, 1975.

18. G. C. Haynes, "The AXMIX Program for Cross-Section Mixing and Library Arrangement," ORNL/TM-5295, December 1974.

19. A. Fabry et al., "Improvement of LWR Prssure Vessel Steel Embrittlement Suveillance: Progress Report on Belgian Activities in Cooperation with the USNRC and other R & D Programs," NUREG/CP-0029, Vol. I, March 1982.

20. W. N. McElroy et al., "Surveillance Dosimetry of Operating Power Plants," NUREG/CP-0029, Vol. I, March 1982.

21. D. L. Phung and W. B. Cottrell, "Analyzing Precursors to Severe Thermal Shock," Nuclear Engineering International, February 1983.

22. P. N. Randal, "Status of Regulatory Demands in the U.S. on the Application of Pressure Vessel Dosimetry," NUREG/CP-0029, Vol. II, March 1982.

23. M. L. Williams, R. Q. Wright and J. Barhen, "Development of Improved Methods for the LWR Lattice Physics Code EPRI-CELL," ORNL/TM-8411, July 1982.

24. W. A. Rhoades and M. B. Emmett, "DOS: The Discrete Ordinates System," ORNL/TM-8362, September 1982.

25. W. Rothenstein, "Resonance Absorption Calculations in Thermal Reactors," Progress in Nuclear Energy, Vol. 5, pp. 95-144, 1980.

26. M. L. Williams, "Correction of Multigroup Cross-Sections for Resolved Resonance Interference in Mixed Absorbers," Nuclear Science and Engineering, 1983.

27. W. Rothenstein, J. Barben, E. Taviv, and M. Aminpour, "Resonance Shielding in Thermal Reactor Lattices: Ann. Nucl. Energy, Vol. 9, pp. 141-168, 1982.

28. M. L. Williams, R. E. Maerker, F. W. Stallman, and F. B. K. Kam, "Validation of Neutron Transport Calculations in Benchmark Facilities for Improved Vessel Fluence Estimation," Presented at the 11th Water Reactor Safety Research Information Meeting, Gaithersburg, Maryland, October 24-28, 1983.

29. F. B. K. Kam, F. W. Stallmann, and M. L. Williams, "Standard Practice for analysis and Interpretation of Physics Dosimetry Results from Test Reactors," Proceedings of the 5th ASTM-EURATOM Symposium on Reactor Dosimetry, Washington, D.C., October 1983.

30. M. L. Williams, "LSU Progress Reports from May 1983 to February 1984," Internal Reports from M. L. Williams to D. G. Cacuci, 1983/84.

Appendix A

TREATMENT OF RESONANCE ABSORPTON IN HETEROGENOUEOUS ASSEMBLIES

A.1 Nordheim Intergral Method[7,8,16]

In contrast to a homogeneous system, the neutron flux in a heterogeneous lattice is not only a function of energy, but strongly depends on position as well. However, the analysis of a heterogeneous lattice can be simplified by first treating each cell separately with no interaction between cells. For each cell, it is assumed that the source flux in the moderator remains flat, even at resonance energies. It is further assumed that this flux is the asymptotic flux, normalized to one source neutron per equivalent cell. The next step is to determine how many of these source neutrons escape capture in slowing down within the cell. For this purpose, it is necessary to set up the neutron-balance equation in both the fuel and the moderator.

For energies in the resonance region, almost all of the slowing down source is due to elastic scattering. Thus neutrons of energy E' may scatter down to $\alpha E'$, and the probability of a neutron at energy E' scattering down to some energy within dE about E is:

$$P(E' \rightarrow E)dE = \left(\frac{1}{1-\alpha}\right)\left(\frac{1}{E'}\right)dE \qquad (A-1)$$

where: $\alpha \equiv \left(\frac{A-1}{A+1}\right)^2$

$A \equiv$ atomic mass

Consider the arrival and departure of neutrons in the energy interval dE in the fuel. As indicated schematically in Fig. A-1, neutrons arrive in dE both as a result of scattering collisions at higher energies in the fuel and by travelling from the moderator into the fuel, having already acquired an energy within dE in the moderator.

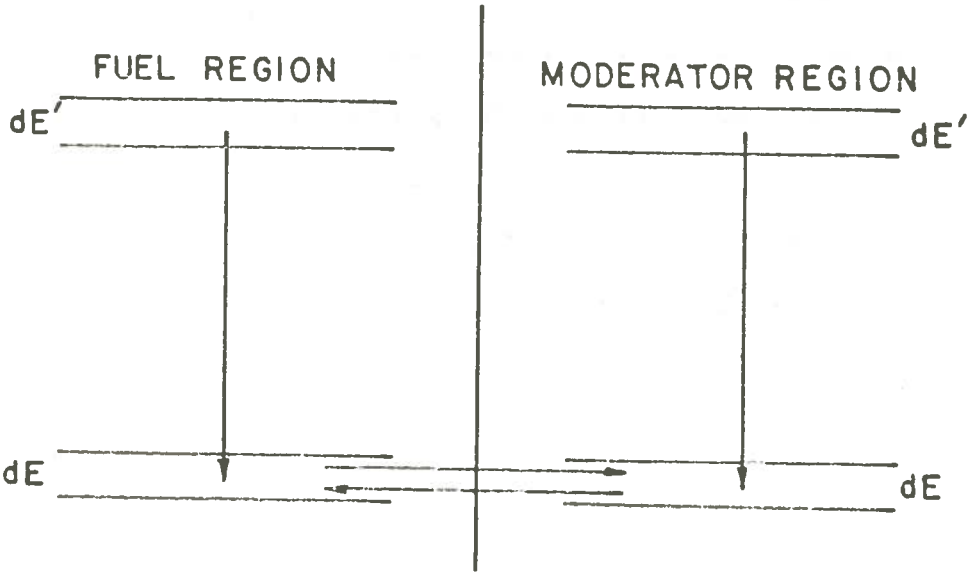

Fig. A-1. Diagram[16] for Deriving the Fuel-Moderator Balance Equation.

The total number of neutrons arriving in dE per volume per second from collisions in the fuel is:

$$V_F dE \int_E^{E/\alpha_F} P(E' \rightarrow E)\, \Sigma_{SF}(E')\, \bar{\Phi}_F(E')dE'$$

$$= \frac{V_F dE}{1-\alpha_F} \int_E^{E/\alpha_F} \Sigma_{SF}(E')\, \bar{\Phi}_F(E')\, \frac{dE'}{E'} \qquad (A-2)$$

where: $V_F \equiv$ volume of fuel in the cell

$$\alpha_F \equiv \left(\frac{A_F-1}{A_F+1}\right)^2$$

$\Sigma_{SF}(E') \equiv$ macroscopic scattering cross-section of the fuel at Energy E'

$\bar{\Phi}_F(E') \equiv$ average flux in the fuel at energy E'

Notice that all these neutrons do not necessarily interact with dE in the fuel, as some neutrons may leave the fuel and have their next interaction in the moderator.

Suppose $P_{FO}(E) \equiv$ probability that a neutron born in the fuel with energy E escapes from the fuel without a collision

Then, $1-P_{FO}(E) \equiv$ probability that this neutron has its next interaction within the fuel

The number of neutrons that are scattered into, and interact in dE in the fuel per volume per second can thus be expressed as:

$$\frac{V_F\left[1-P_{FO}(E)\right]dE}{1-\alpha_F}\int_E^{E/\alpha_F}\Sigma_{SF}(E')\bar{\Phi}_F(E')\frac{dE'}{E'} \qquad (A-3)$$

Now, suppose $P_{MO}(E) \equiv$ probability that a neutron of energy E in the moderator has its next collision in the fuel

The number of neutrons arriving in dE from the moderator can thus be expressed as:

$$\frac{V_M\ P_{MO}(E)dE}{1-\alpha_M} \int_E^{E/\alpha_M} \Sigma_{SM}(E')\ \bar{\Phi}_M(E')\ \frac{dE'}{E'} \qquad \text{(A-4)}$$

where: $V_M \equiv$ volume of moderator in the cell

$$\alpha_M \equiv \left(\frac{A_M-1}{A_M+1}\right)^2$$

$\Sigma_{SM}(E') \equiv$ macroscopic scattering cross-section of the fuel at energy E'

$\bar{\Phi}_M(E') \equiv$ average flux in the fuel at energy E'

By adding Eqs. (A-3) and (A-4), we get the neutron-balance equation for the fuel, i.e.

$$V_F\ \Sigma_{tF}(E)\ \bar{\Phi}_F(E) = \frac{V_F[1-P_{FO}(E)]dE}{1-\alpha_F} \int_E^{E/\alpha_F} \Sigma_{SF}(E')\bar{\Phi}_F(E')\ \frac{dE'}{E'}$$

$$+ \frac{V_M\ P_{MO}(E)}{1-\alpha_M} \int_E^{E/\alpha_M} \Sigma_{SM}(E')\bar{\Phi}_F(E')\ \frac{dE'}{E'} \qquad \text{(A-5)}$$

where

$\Sigma_{tF}(E) \equiv$ total macroscopic cross-section of the fuel at energy E

$\bar{\Phi}_F(E) \equiv$ average flux in the fuel at energy E

In a similar manner, the neutron-balance equation for the moderator can be derived. Since there is almost no absorption of neutrons in the moderator at resonance

energies, the total cross-section is approximately equal to the scattering cross-section (i.e. $\Sigma_{tM} \approx \Sigma_{sM}$).

The neutron-balance equation for the moderator can thus be expressed as:

$$V_M \Sigma_{sM}(E) \bar{\Phi}_M(E) = \frac{V_F P_{FO}(E)}{1-\alpha_F} \int_E^{E/\alpha_F} \Sigma_{SF}(E') \bar{\Phi}_F(E') \frac{dE'}{E'} + \frac{V_M [1-P_{MO}(E)]}{1-\alpha_M} \int_E^{E/\alpha_M} \Sigma_{SM}(E') \bar{\Phi}_M(E') \frac{dE'}{E'} \qquad (A-6)$$

Notice that Eqs (A-5) and (A-6) constitute a set of coupled integral equations where $\bar{\Phi}_F(E)$ and $\bar{\Phi}_M(E)$ are dependent on one-another.

In order to compute the fluxes using the above balance equations, it is necessary to specify the probabilities P_{FO} and P_{MO}. The assumption that the scatter sources are flat in the fuel and moderator respectively serves this purpose. This assumption satisfies our purposes because the errors caused by the assumption are cancelled out, as will be seen later.

With the assumption that sources are flat in the fuel and moderator, and using the "reciprocity theorem," it can be shown that P_{FO} and P_{MO} are related by the following equation:

$$P_{FO}\,\Sigma_{tF}\,V_F = P_{MO}\,\Sigma_{SM}\,V_M \qquad \text{(A-7)}$$

Before considering the detailed solution of Eqs. (A-5) and (A-6), it is convenient to note that the asymptotic solutions (i.e. the asymptotic fluxes in the absence of absorptions) are the same in the fuel and moderator. Representing these solutions by Φ_F^∞ and Φ_M^∞ respectively, it can be shown by direct substitution, and the use of Eq. (A-7) that:

$$\Phi_F^\infty = \Phi_M^\infty = \frac{1}{\overline{\xi\Sigma}_p E} = \frac{1}{\overline{\xi\Sigma}_s E} \qquad \text{(A-8)}$$

and

$$\overline{\xi\Sigma}_s = \frac{1}{V}\left(\xi_F \Sigma_{SF} V_F + \xi_M \Sigma_{SM} V_M\right) \qquad \text{(A-9)}$$

where: $\Sigma_{PF} \equiv$ potential scattering cross-section of the fuel

$\Sigma_{SF} \equiv$ scattering cross-section of the fuel

$V \equiv V_F + V_M \equiv$ total volume of the cell

$\overline{\xi} \equiv$ average logarithmic energy decrement

$\overline{\Sigma}_S \equiv$ average scattering cross-section

Note: In the asymptotic region, far from resonances,

$$\Sigma_{PF} = \Sigma_{SF}$$

With the knowledge of the asymptotic solutions, we can now invoke the Narrow Resonance (NR) approximation for the moderator. It is possible to decouple the heterogeneous balance equations by observing that the energy loss per

collision with the moderator is usually small compared to the practical width of the resonances in the fuel. This essentially points to the fact that at energies E' just above the resonance, there is very little absorption, and the flux there assumes the asymptotic form:

$$\bar{\Phi}_F(E') = \Phi_M^{\infty} = \frac{1}{\xi \sum_s E'} \tag{A-10}$$

Also notice that $\sum_{SM}$ becomes a constant at resonance energies. Thus, the second term on the R.H.S. of Eq. (A-5) can be written as:

$$\frac{V_M P_{MO}(E)}{1-\alpha_F} \int_E^{E/\alpha_M} \sum_{SM}(E') \Phi_M(E') \frac{dE'}{E'} = \frac{V_M P_{MO}(E) \sum_{SM}}{\xi \sum_s E} \tag{A-11}$$

Making use of Eq. (A-7), we can express the R.H.S. of Eq. (A-11) as:

$$\frac{V_M P_{MO}(E) \sum_{SM}}{\xi \sum_s E} = \frac{V_F P_{FO}(E) \sum_{tF}(E)}{\xi \sum_s E} \tag{A-12}$$

The neutron-balance expression of Eq. (A-5) now reduces to:

$$\sum_{tF}(E) \Phi_F(E) = \frac{1-P_{FO}(E)}{1-\alpha_F} \int_E^{E/\alpha_F} \sum_{SF}(E') \Phi_F(E') \frac{dE'}{E'} + \frac{P_{FO}(E) \sum_{tF}(E)}{\xi \sum_s E} \tag{A-13}$$

Eq. (A-13) shows that, on the basis of the flat source assumption, the flux in the fuel is determined by one integral equation. Furthermore, it can be observed that P_{FO} appears in Eq. (A-13) with both signs, consequently, any error in P_{FO} tends to cancel out in the flux calculation. The expression of Eq. (A-13) can be solved by using standard numerical methods.

A.2 Narrow Resonance (NR) Approximation[8,16]

If the average energy loss in an elastic collision with the fuel is large, compared with the practical width of a resonance, it is very unlikely that a neutron will have a second collision within the resonance and be absorbed. It is then possible to replace the flux in the integral of Eq. (A-13) by its asymptotic form, as depicted in Eq. (A-10). The integration can then be computed, noting that the scattering cross-section of the fuel in the integral has to be replaced by its constant potential scattering. This takes into account the fact that in the NR approximation, neutrons are scattered down into the resonance from energies above the resonance (i.e. where $\bar{\Sigma}_{SF} = \bar{\Sigma}_{PF}$).

Eq. (A-13) now becomes:

$$\Sigma_{tF}(E)\ \bar{\Phi}_F(E) = \frac{1}{1-\alpha_F}\ \frac{\Sigma_{PF}}{\xi\Sigma_s E}\ \int_E^{E/\alpha_F}\ [1-P_{FO}(E)]\ \frac{dE'}{(E')^2}$$

$$+\ \frac{P_{FO}(E)\Sigma_{tF}(E)}{\xi\Sigma_P\ E}$$

$$= \frac{1-P_{FO}(E)}{1-\alpha_F}\ \frac{\Sigma_{PF}}{\xi\Sigma_P}\ \frac{1-\alpha_F}{E}\ +\ \frac{P_{FO}(E)\Sigma_{tF}(E)}{\xi\Sigma_P\ E}$$

$$= \frac{1}{\xi\Sigma_P\ E}\left[\ [1-P_{FO}(E)]\ \Sigma_{PF} + P_{FO}(E)\ \Sigma_{tF}(E)\right] \qquad \text{(A-14)}$$

A.3 Narrow Resonance Infinite Mass (NRIM) Approximation[16]

At resonances (particularly low energy resonances), where the average energy loss in a scattering collision with the absorber is not large, compared with the practical width, it is reasonable to ignore scattering by the absorber altogether. This is equivalent to assuming that the average energy loss approaches zero as the mass of the absorber becomes large.

For a heterogeneous lattice, a neutron may now undergo repeated scattering in the fuel within a single resonance before escaping. Assuming that the collision density is independent of position for all collisions, the

total escape probability P_F can be computed by considering a succession of collisions of the neutrons in the fuel. If N neutrons are uniformly produced in the fuel lump, the total number of neutrons escaping is:

$$NP_{FO} + N(1-P_{FO}) \frac{\sigma_{SF}}{\sigma_{tF}} P_{FO} + N(1-P_{FO})^2 \left(\frac{\sigma_{SF}}{\sigma_{tF}}\right)^2 P_{FO} + \ldots \quad \text{(A-15)}$$

where the first term is without collision, the second term is the first collision, the third term is the second collision, and it goes on in that order.

From Eq. (A-15), the total escape probability is:

$$P_F = \frac{P_{FO}}{1-(1-P_{FO}) \frac{\sigma_{SF}}{\sigma_{tF}}} \quad \text{(A-16)}$$

To use NRIM approximation, we simply replace P_{FO} in Fig. (A-13) by P_F from Eq. (A-16).

A.4 Resonance Absorption in Closely Packed Lattices[7,16]

Up to this point, we have only treated the case in which the fuel lumps are so widely spaced, with the assumption that they do not interact with each other (i.e. neutrons with energies in the resonance region do not pass from one fuel lump to another). On the basis of this assumption, the escape probability from a single fuel lump P_{FO} was defined as the probability that a neutron in the lump will have its next collision in the moderator.

However, if the fuel lumps interact, as in the VENUS configuration, the next collision may take place in another fuel lump. Thus, we now define an effective escape probability P^*_{FO} for close lattices, with identical meaning; i.e. probability that a neutron born with a flat distribution in an absorber makes its next collision in the moderator, excluding the cases in which, after traversal of one or more moderator sections, it collides inside another fuel lump. Notice that under the flat-source assumption, all previous formulas still hold when P_{FO} is replaced by P^*_{FO}, and it is only a matter of finding the appropriate expression for P^*_{FO}.

As one may have guessed, it is more difficult to compute the escape probability for an interacting lattice than for an isolated fuel lump. An approximate formula for P^*_{FO} is given by:

$$P^*_{FO}(E) = P_{FO}(E)\left[\frac{1-C}{1-\left[1-\bar{r}\,\Sigma_{tF}\,P_{FO}(E)\right]}\right] \qquad \text{(A-17)}$$

where: $\bar{r} \equiv$ average chord length in one fuel lump

$C \equiv$ Dancoff-Ginsberg correction factor for the lattice

In terms of P^*_{FO}, Eq. (A-13) now becomes:

$$\Sigma_{tF}(E)\ \bar{\Phi}_F(E) = \frac{1-P^*_{FO}(E)}{1-\alpha_F}\ \int_E^{E/\alpha_F} \Sigma_{SF}(E')\ \bar{\Phi}_F(E')\ \frac{dE'}{E'} + \frac{P^*_{FO}(E)\Sigma_{tF}(E)}{\overline{\xi\Sigma_s}\ E} \qquad \text{(A-18)}$$

A.5 Implementation of Nordheim's Integral Method in NITAWL[8]

The integral expression of Eq. (A-18) is the basis of the Nordheim method that was used in the VENUS calculation. This equation is slightly modified into a form that is subsequently implemented in the NITAWL code.

Suppose, we define the maximum fractional energy loss per collision as:

$$\alpha^*_F = 1-\alpha_F \qquad \text{(A-19)}$$

Substituting Eq. (A-19) into Eq. (A-18), we have:

$$\Sigma_{tF}(E)\ \bar{\Phi}_F(E) = \frac{1-P^*_{FO}(E)}{\alpha^*_F}\ \int_E^{E/1-\alpha^*_F} \Sigma_{SF}(E')\ \bar{\Phi}_F(E')\ (\frac{1}{E'})dE' + P^*_{FO}(E)\ \Sigma_{tF}(E)\ \frac{1}{\overline{\xi\Sigma_s}}\ (\frac{1}{E}) \qquad \text{(A-20)}$$

Additional nuclides in the fuel or moderator are accounted for by adding the necessary integrals. The NITAWL code allows up to three such integrals--one for

the absorber and two for the non-resonance nuclides in the fuel.

Eq. (A-20) can now be written in the following form:

$$\Sigma_{tF}(E)\bar{\Phi}(E) = \sum_{i=1}^{3}\left[\frac{1-P^{*}_{FO}(E)}{\alpha^{*}_{Fi}}\int_{E}^{E/1-\alpha^{*}_{Fi}}\Sigma^{i}_{SF}(E')\bar{\Phi}_{F}(E')\left(\frac{1}{E'}\right)dE'\right.$$

$$\left. + P^{*}_{FO}(E)\ \Sigma^{i}_{tF}(E)\ \frac{1}{\bar{\xi}\Sigma_{s}}\ \left(\frac{1}{E}\right)\right] \qquad \text{(A-21)}$$

where i is the nuclide index:

i = 1 for the absorber

i = 2 for the first admixed moderator in the fuel

i = 3 for the second admixed moderator in the fuel

The NITAWL code assumes that the resonances are well isolated (without overlap), and it employs the asymptotic solution for the flux between resonances. In addition, it assumes the asymptotic value for the flux at the upper end of each resonance.

Realize that the flux spectrum in an isolated fuel lump is independent of the material properties of the surrounding moderator, and that the NITAWL code does in fact solve Eq. (A-18) with no knowledge of surrounding moderator properties. This is because the asymptotic treatment of the flux at the upper end of each resonance

gives rise to the term $\overline{\xi\Sigma}_s$ on the R.H.S. of Eq. (A-21), and which eventually cancels out when the group averaged cross-section is determined.

Thus, we can eliminate the term $\overline{\xi\Sigma}_s$ from Eq. (A-21), i.e.

$$\Sigma_{tF}(E)\bar{\Phi}(E) = \sum_{i=1}^{3}\left[\frac{1-P^{*}_{FO}(E)}{\alpha^{*}_{Fi}}\int_{E}^{E/1-\alpha^{*}_{Fi}}\Sigma^{i}_{SF}(E')\bar{\Phi}_F(E')\left(\frac{1}{E'}\right)dE' + P^{*}_{FO}(E)\,\Sigma^{i}_{tF}(E)\left(\frac{1}{E}\right)\right] \qquad \text{(A-22)}$$

Since the neutron flux in the moderator region is a function of energy, we can express Eq. (A-22) in the following form:

$$\Sigma_{tF}(E)\bar{\Phi}(E) = \sum_{i=1}^{3}\left[\frac{1-P^{*}_{FO}(E)}{\alpha^{*}_{Fi}}\int_{E}^{E/1-\alpha^{*}_{Fi}}\Sigma^{i}_{SF}(E')\bar{\Phi}_F(E')\left(\frac{1}{E'}\right)dE' + P^{*}_{FO}(E)\,\Sigma^{i}_{tF}(E)\,W(E)\right] \qquad \text{(A-23)}$$

where W(E) is the assumed energy variation of the neutron flux in the moderator region. In the thermal range, W(E) is equal to the Maxwellian distribution, and in the resonance range, W(E) is equal to $\frac{1}{E}$.

The expression of Eq. (A-23) was used in the NITAWL code to perform resonance shielding calculations for the VENUS analysis. The resonance materials encountered in the VENUS configuration are U-235 and U-238.

The NITAWL[8,9] code numerically computes the expression of Eq. (A-23), using the following sequential procedure:

1. The equations for the collission density are converted from the energy variable into the lethargy variable (i.e. $u = \ln(E'/E)$). The macroscopic cross-sections are divided by the atom density of the absorber, thereby normalizing the collision density to one absorber atom.
2. Each resonance is treated separately, thus allowing the determination of an energy E' above each resonance at which an asymptotic slowing down flux is assumed. On the basis of the slowing-down interval of the absorber, an integration mesh is defined for each resonance. The scattering cross-sections of the admixed moderators are

adjusted to produce the correct slowing-down sources when integrated over this mesh.

3. Using the asymptotic source from above each resonance as a starting point, a reverse integration (from the highest to the lowest energy) by Simpson's rule summation is performed to obtain the variation of the collision density across the resonance.
4. At each lethargy interval, point values of the resonance cross-sections and the effective escape probability for the absorber are calculated for use in determining the collision density.
5. Finally, the flux distribution associated with the calculated collision density is used as a weighting function to average the reaction cross-sections over the various energy groups.

Appendix B

DISCRETE ORDINATES TREATMENT OF TRANSPORT THEORY

B.1 Choice of Transport Theory over Diffusion Theory

Over the years, reactor analysis have been performed largely with the method of diffusion theory. Whereas difussion theory has proved to be adequate for many reactor calculations (involving reasonably large homogeneous region) it is clearly deficient when applied to certain class of problems.

Diffusion theory is based on the assumption that neutron scattering is linearly anisotropic and that neutron flux changes slowly with position. But these two assumptions are clearly violated when applied to deep penetration problems where anisotropic effects with rapidly changing flux can dominate. In effect, the diffusion theory is inadequate (if not redundant) for problems of this type, instead, a more rigorous method, such as the transport theory is required for better accuracy. The diffusion theory method can probably be used to perform in-core calculations for the VENUS configuration but with less accuracy, relative to the transport theory method. As for the ex-core calculations, difficusion theory is ineffective,

due to non-linear anistropic scattering, and rapid flux variations.

B.2 Neutron Balance Condition

The analysis of a reactor core requires a knowledge of its neutron-balance condition. The state of the neutron-balance is the condition that exist when the total rate of neutron production is equal to the total rate of neutron depletion. Neutron production can be due to fission sources, external fixed sources, and scatter from other energies and/or directions. Neutron depletion can be due to absorption, leakage, and scatter to other enregies and/or directions.

In transport theory, the neutron balance condition is applied to the number of neutrons within any small volume (dV) in space, within any narrow energy interval (dE) and travelling within a narrow solid angle ($d\Omega$) of direction vectors.

B.3 Boltzmann Transport Equation[17]

The mathematical expression which states the balance of neutron losses and productions in terms of space, energy, and direction dependent neutron flux and cross-section is called the Boltzmann transport equation. The transport equation can be written in several forms, and depends on the

type of coordinate system that is being used to describe the reactor system.

The steady-state time independent integro-differential balance equation can be written as:

$$\Omega \cdot \nabla \psi(r,E,\Omega) + \Sigma_t(r,E)\psi(r,E,\Omega)$$

$$= \int_{E'} dE \int_{4\pi} d\Omega' \left[\sum_i \chi^i(E) \nu^i \Sigma_f^i(r,E') \right.$$

$$\left. + \Sigma_s(r,E' \rightarrow E, \Omega' \rightarrow \Omega) \right] \psi(r,E',\Omega') + Q(r,E,\Omega) \qquad \text{(B-1)}$$

where $\Omega \equiv$ direction vector

$\nabla \equiv$ differential operator

$\psi(r,E,\Omega), \psi(r,E',\Omega') \equiv$ angular fluxes

$\chi^i(E) \equiv$ fission spectrum for isotope i

$\nu^i \equiv$ average number of fission neutrons for isotope i

$\Sigma_f^i(r,E') \equiv$ macroscopic fission cross-section

$\Sigma_s(r,E' \rightarrow E, \Omega' \rightarrow \Omega) \equiv$ macroscopic scattering cross-section per unit energy for scattering from energy E' to E and from direction Ω' to Ω

$Q(r,E,\Omega) \equiv$ fixed source

The first term on the L.H.S. of Eq. (B-1) is due to leakage while the second term is due to absorption and scatter-out. The first term on the R.H.S. is due to fission source, the

second term is due to scatter-in, and the third term is due to fixed sources.

Eq. (B-1) is the steady-state Boltzmann transport equation for the angular flux. If this equation can be efficiently solved for the material and geometrical configurations of interest, the accuracy of the reactor physics analysis would be limited only by the accuracy of the cross-sections used.

B.4 Discrete Ordinates (or S_n) Method

There are two general methods which are most commonly used in solving the transport equation. One is called the Monte Carlo method, which is based on statistically simulating the particle (e.g. neutron) paths through the region of interest. The other is called the discrete ordinates method, and it employs deterministic approach.

The S_n method (first introduced by B. G. Carlson in 1958), is a procedure for determining numerical solutions to the Boltzmann transport equation. The basis of the discrete ordinates method is to express the continuous form of the Boltzmann equation in terms of discrete variables, where the spatial variables are expressed as finite intervals, the energy variables as energy groups, and the direction variables as discrete directions. While the continuous transport equation represents a neutron balance over

differential intervals (dV, dE, dΩ), the discrete ordinates equation represents a neutron balance over finite intervals. The discrete abscissas that define the finite intervals are called mesh points for space intervals, group boundaries for energy intervals, and quadrature sets for discrete directions. The discrete ordinates corresponding to these discrete abscissas represent the average (or integrated) angular flux over the corresponding interval in space, energy and direction. Anistropic scattering is treated by using Legendre polynomials.

B.5 A One-Dimensional Discrete Ordinates Method - XSDRNPM[10]

A one-dimensional computation of a system simply means that calculations are at points along one axis, where the system is assumed to extend to infinity along the other axes. Three major types of coordinate system are shown in Fig. B-1.

The time-independent Boltzmann equation can be reduced with a one-dimensional coordinate system of interest. In the case of a slab, suppose calculations are along the x-axis, then there is no leakage in both the y-axis and z-axis. As for a cylinder, the length along the z-axis is infinite and the calculation is for points located at distance "r" from the median axis. Similarly for a sphere,

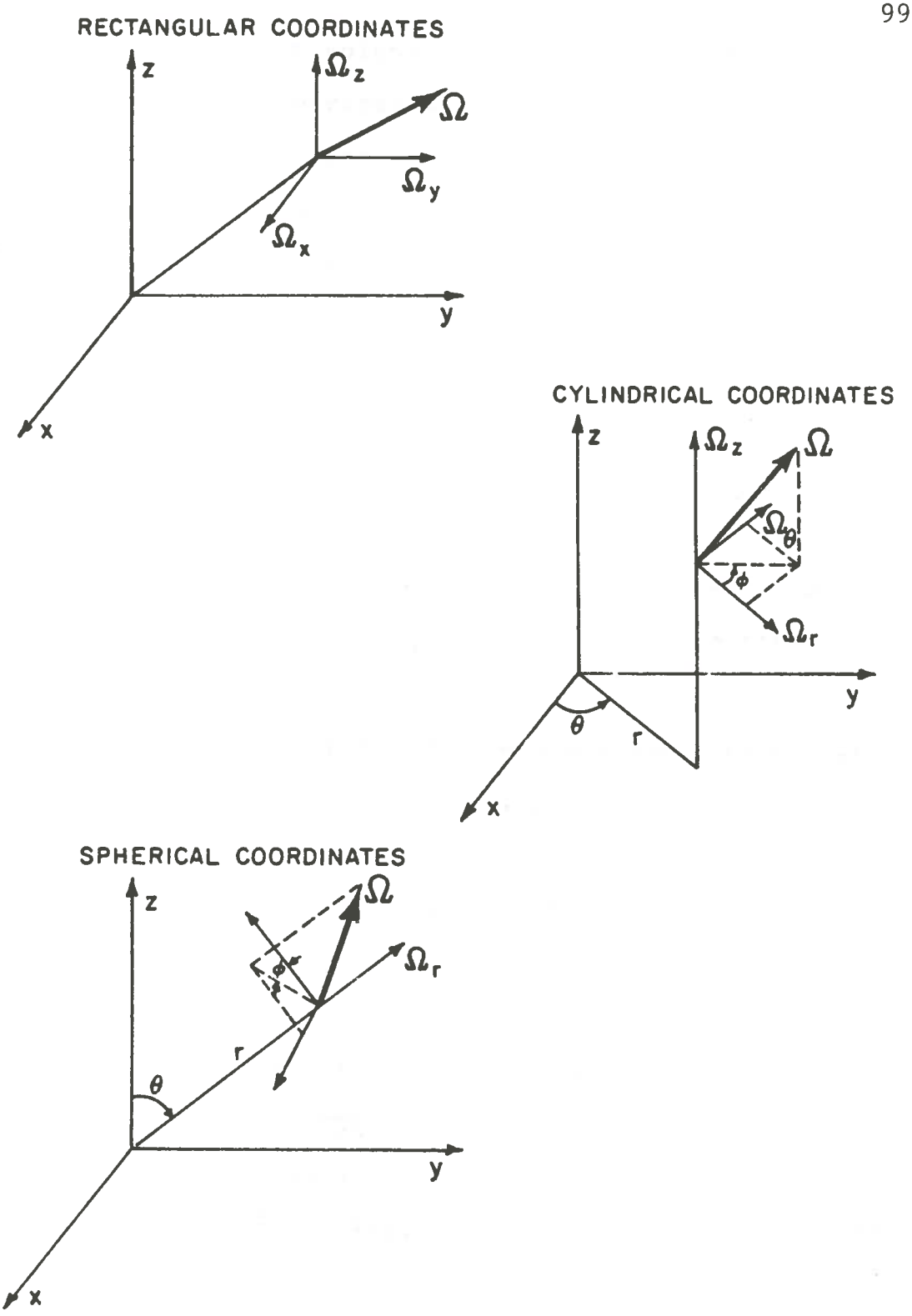

Fig. B-1. Three Major Coordinate Systems.

the calculation is at points located at distance "r" from the center of the spherical system.

Illustrations of the one-dimensional coordinate system for slab, cylinder, and sphere are shown in Fig.B-2. Notice that the directions are cones in the case of slab and sphere, whereas, in the case of cylinder, the same simple symmetries do not hold (i.e, a cone around the radius does not strike the next cylindrical shell at the same distance from a point on a radius), and the directions must be specifically described. However, there are many symmetries in the one-dimensional cylinder which allow one to only describe direction for one quadrant of the direction sphere about a point.

As mentioned earlier, the one-dimensional geometries allow simplification of Eq. (B-1), particularly in the leakage term. It is normal to calculate as a function of angles expressed in cosine units, i.e,

$$\mu = \cos \Phi \tag{B-2}$$

$$\eta = \cos \zeta \tag{B-3}$$

Thus, for a slab, we can write the leakage term as:

$$\Omega \cdot \nabla \psi(r,E,\Omega) = \mu \frac{\partial}{\partial x} \psi(x,E,\mu) \tag{B-4}$$

For a cylinder, we have:

$$\Omega \cdot \nabla \psi(r,E,\Omega) = \frac{\mu}{r} \frac{\partial}{\partial r} \left[r \psi(x,E,\mu,\eta) \right] - \frac{1}{r} \frac{\partial}{\partial \Phi} \left[\eta \psi(x,E,\mu,\eta) \right] \tag{B-5}$$

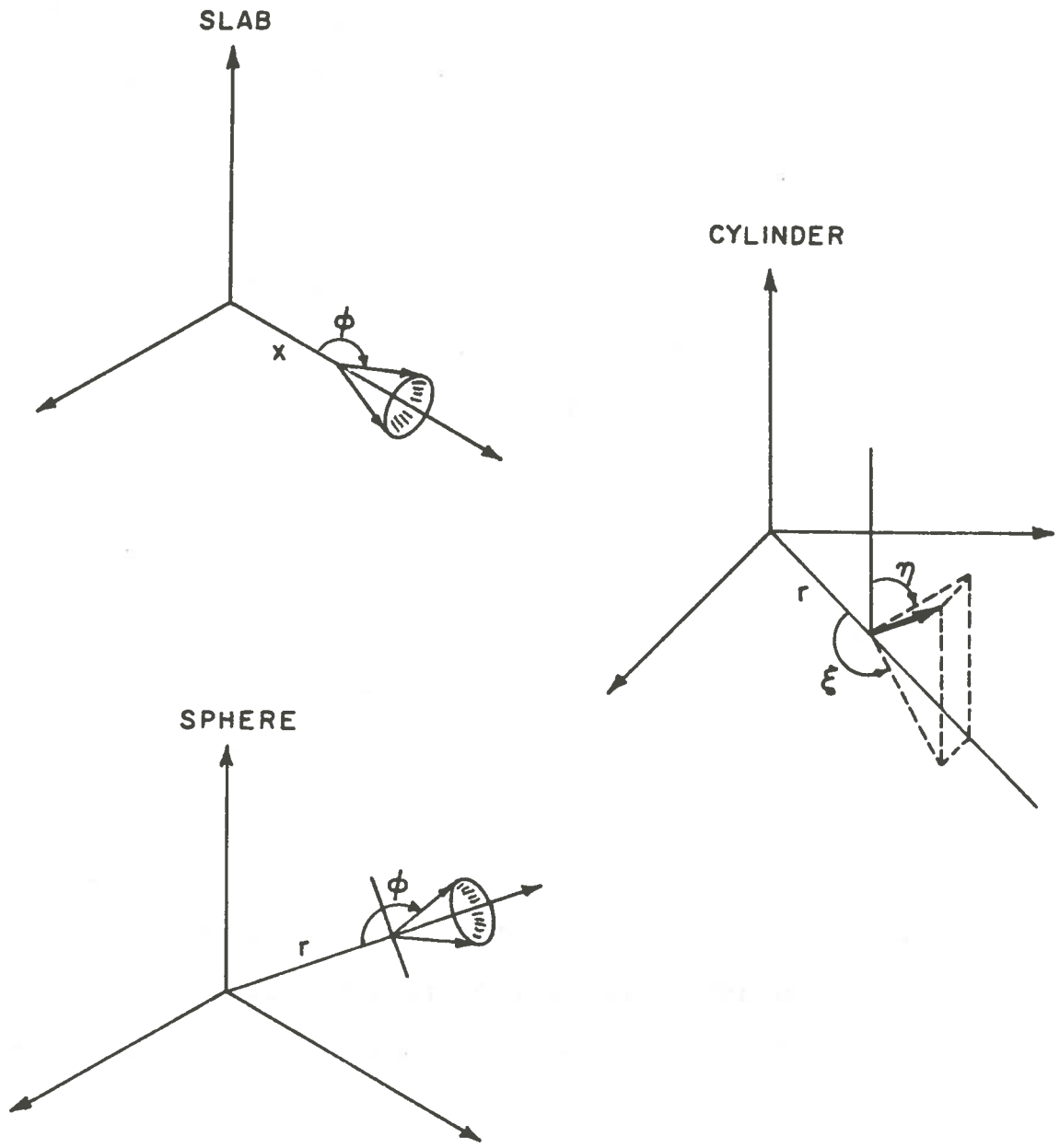

Fig. B-2. Three 1-D Coordinate Systems.

And finally, for a sphere, we have:

$$\Omega \cdot \nabla \psi(r,E,\Omega) = \frac{\mu}{r^2} \frac{\partial}{\partial r} \left[r^2 \psi(r,E,\mu) \right] + \frac{1}{r} \frac{\partial}{\partial \mu} \left[(1-\mu^2) \psi(r,E,\mu) \right] \quad \text{(B-6)}$$

XSDRNPM is a discrete ordinates transport code which numerically solves the one-dimensional Boltzmann equation in slab, cylinder or spherical coordinates. It performs spatial cross-section weighting, and in addition, it uses the fluxes determined from its spectral calculation to collapse input cross-sections.

A considerable amount of flexibility is allowed in describing a problem for XSDRNPM. The number of spatial intervals, energy groups, quadrature set, and the order of fits to the angular variation in basic cross-sections are all arbitrary and are limited only by economic factors.

The flux calculation can be performed according to several options, including fixed source calculations, eigenvalue calcuations, and dimension search calculations. Also it allows for a variety of weighting options as described below:

1. Cell weighting - generates cross-sections consistent with mocking-up a cellular configuration as a homogenized region - spatial disadvantage factors are taken into account in the cross-section weighting.

2. Zone weighting - produces a set of weighted cross-sections which preserves the reaction rates for each zone.
3. Region weighting - generates one set of cross-sections for a nuclide, but weighted over a composite spectrum made up of all spectra from regions where the nuclide is present.
4. Inner cell weighting - performs a cell weighting over specified innermost regions, and nuclides outside these regions are not weighted.

A cell is defined as being a unit cell component of the heterogeneous lattice as depicted by Fig. IV-1. A zone is a volume element in which the same macroscopic cross-sections are used at each interval. A region is a collection of zones, used primarily for defining output edits.

In the VENUS analysis, the cell weighting option was used in cell averaging the 3.3% and 4.0% fuel cross-sections, the inner-cell weighting option was used in determining the spatially weighted pyrex cross-sections, and the zone weighting option was used in collapsing the 218 group cross-sections into 10 group cross-sections.

A comprehensive description of XSDRNPM can be found in Reference 10.

B.6 A Two-Dimensional Discrete Ordinates Method - DOT IV[12]

DOT IV is the latest in the series of discrete ordinates transport (DOT) codes developed at ORNL. DOT IV is continuously evolving, and periodically a new version is released. The most up-to-date version available to the public at this time is called DOT IV.3, and it represents significant improvements over the earlier versions of the DOT code. This latest version of DOT IV is the basis of the description contained herein.

DOT IV has a variety of applications including eigenvalue calculation and fixed source calculations which were used in the present study.

The time-independent Boltzmann transport equation is numerically solved by DOT IV to determine the flux or fluence of particles (e.g. neutrons) in one or two dimensional geometry. The transport equation is solved for the flow of particles moving in a set of discrete directions in each cell of a space mesh, and in each group of a multigroup energy structure. Iterations are performed until convergence is attained. Fundamentally, the expression of Eq. (B-1) is reduced with the geometry of interest (e.g. 2-D), then formulated as a finite-difference equation, and theoretically the solutions approach the exact solution of the Boltzmann equation, as space, energy, and angular meshes approach differential size.

The discrete mesh intervals are defined by specifying the corners of the finite intervals that constitute the mesh. The 2-D spatial mesh can be specified by X-Y, R-Z, and R-θ geometries. An X-Y geometry is a subset of a 3-D Cartesian coordinate system, and flux is assumed to be flat along the unspecified third dimension. The computed 2-D fluxes are on per unit distance basis in the third dimension. An X-Y geometry shown in Fig. B-3 was used in the VENUS core calculations. The parameters A^V and A^H in the figure are cell areas perpendicular to the respective axis of interest (i.e. vertical and horizontal axes).

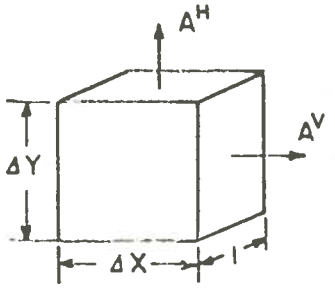

$$A^V = \Delta Y \qquad A^H = \Delta X \qquad V = (\Delta X)(\Delta Y)$$

Fig. B-3. DOT IV X-Y Mesh Element.

The discrete energy mesh is the dimension of the energy range of interest into energy groups, as dictated by the

cross-section set input to DOT IV. Ten energy groups and 56 energy groups were used in the VENUS calculations.

In the discrete ordinates method, integrals over direction space are replaced with weighted sums over sets of discrete directions. The directions are represented by their direction cosines (μ, η, ξ) with respect to a set of orthogonal coordinate axes. The direction vectors are represented graphically in Fig. B-4.

With $\vec{i}$, $\vec{j}$, $\vec{k}$ as unit vectors along the axes, the discrete direction set is

$$\mu_m \vec{i} + \eta_m \vec{j} + \xi_m \vec{k} \quad , \; 1 \leq m \leq mm \tag{B-7}$$

where: $mm \equiv$ total number of discrete directions

$\mu \equiv \Omega_x \equiv \sin \alpha \cos \Phi$

$\eta \equiv \Omega_y \equiv \cos \alpha$

$\xi \equiv \Omega_z \equiv \sin \alpha \sin \Phi$

Associated with each discrete direction is the directional weight W_m, which is equal to a fraction of the surface area of a unit sphere, i.e.

$$W_m = \frac{\Delta\Omega_m}{4\pi} \tag{B-8}$$

where: $\Omega_m \equiv$ a discrete direction

$\Delta\Omega_m \equiv$ the area associated with a discrete direction

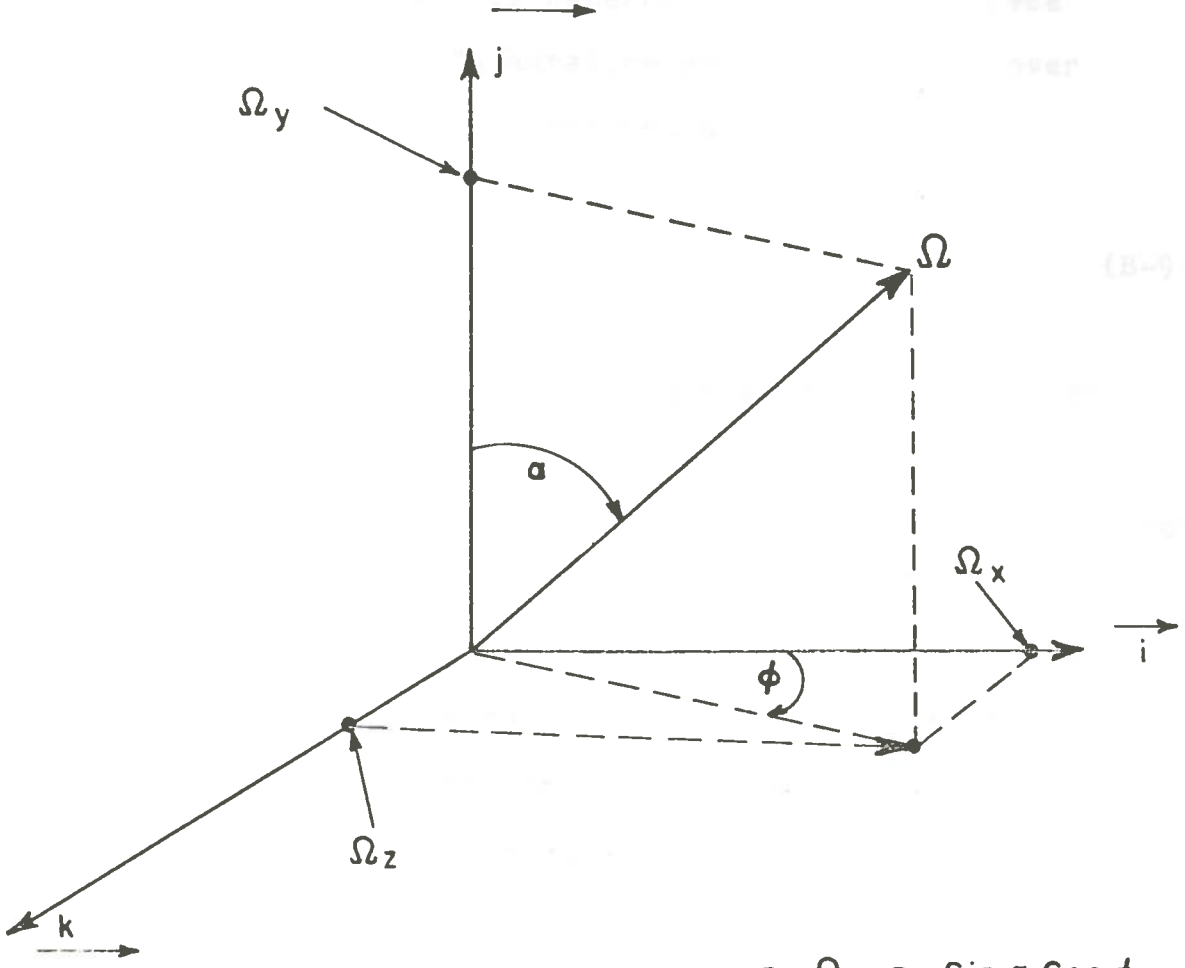

$$\mu = \Omega_x = \sin\alpha \cos\phi$$

$$\eta = \Omega_y = \cos\alpha$$

$$\xi = \Omega_z = \sin\alpha \sin\phi$$

$$\Omega = \Omega_x \vec{i} + \Omega_y \vec{j} + \Omega_z \vec{k}$$

Fig. B-4. Neutron Direction Vector Expressed in Direction Cosines.

The set of discrete directions (Ω_m) together with their associated weights (W_m) is referred to as the discrete ordinates directional "quadrature set." Integrals over direction space can be represented as:

$$\int f(\Omega)d\Omega \approx \sum_{m=1}^{mm} W_m \, f(\mu_m, \eta_m, \xi_m) \qquad \text{(B-9)}$$

The quadrature set is constrained by the following:

$$\sum_{m=1}^{mm} W_m = 1 \qquad \text{(B-10)}$$

$$\mu_m^2 + \eta_m^2 + \xi_m^2 = 1 \qquad \text{(B-11)}$$

The fundamental variable of 2-D DOT IV neutron transport calculation is the angular flux, i.e.

$$\psi(x,y,E,\Omega) = v\, N(x,y,E,\Omega) \qquad \text{(B-12)}$$

where: $v \equiv$ neutron speed

$N \equiv$ angular neutron density

Although angular flux is the primary mode of DOT IV calculation, it is necessary to transform it into a more useful form called the scalar flux. The scalar flux can be defined as the integral of the angular flux over all directions, i.e.

$$\Phi(x,y,E) = \int_{4\pi} \psi(x,y,E,\Omega)d\Omega \qquad \text{(B-13)}$$

The transport equation solved by the discrete ordinates method contains a scattering term in which the macroscopic scattering cross-section relates the scatter of particles from energy E' and direction Ω' to energy E and direction Ω. The change in the neutron direction before and after a collision is usually expressed in terms of the angle between the initial and final unit direction vectors. The scattering angle is represented graphically in Fig. B-5.

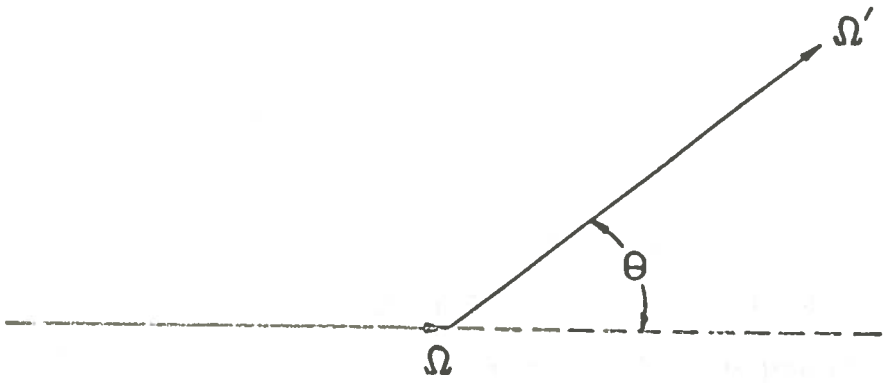

$\mu_0 = \cos\theta$

θ = Scattering Angle
Ω = Initial Direction
Ω' = Final Direction

Fig. B-5. Definition of Neutron Scattering Angle.

Using the definition of the dot (or inner) product of two unit vectors,

$$\Omega' \cdot \Omega = \text{Cos } \theta \qquad \text{(B-14)}$$

where θ is the scattering angle

Define $$\mu_0 = \text{Cos } \theta \qquad \text{(B-15)}$$

The scattering cross-section in the scattering term of Eq. (B-1) can be written as:

$$\sum_s (E' \rightarrow E, \ \Omega' \rightarrow \Omega) = \sum_s (E' \rightarrow E, \mu_0)$$

Anisotropic scattering is treated in DOT IV by expanding the angle dependent scattering cross-section in Legendre polynominals of the scatter cosine (i.e., μ_0). Legendre polynominals are simply functions of powers of μ_0. An n-th order Legendre polynomial is a polynomial of order n that contains μ_0^n, and it is usually denoted by $P_N(\mu_0)$. Hence an n-th order Legendre expansion of the scattering cross-section is synonymous to expressing the angle dependent cross-section as an n-th order polynomial in μ_0, i.e.,

$$\sum_s (E' \rightarrow E, \mu_0) = A_0 + A_1 \mu_0 + A_2 \mu_0^2 + \ . \ . \ . \ + A_n \mu_0^n \qquad \text{(B-16)}$$

where the coefficients A_0, A_1, A_2 ..., A_n are generally functions of E' and E.

In most transport calculations as in the VENUS case, a 3rd order Legendre expansion has been found to be sufficient. For a 3rd order Legendre expansion, the angle dependent scattering cross-section can be written as:

$$\sum_s(E'\rightarrow E,\mu_0) = \sum_0(E'\rightarrow E)\ P_0 + \sum_1(E'\rightarrow E)\ P_1(\mu_0)$$

$$+ \sum_2(E'\rightarrow E)\ P_2(\mu_0)\ \sum_3(E'\rightarrow E) + P_3(\mu_0) \qquad \text{(B-17)}$$

The coefficients of the Legendre polynomials are called the "cross-section moments." In the DOT IV methodology, each of the cross-section moment is represented as a separate material in the cross-section library, thus in a 3rd order Legendre expansion, four materials are present for each nuclide. The cross-section moments of physical significance are the P_0 and P_1. The matrix $\sum_1(E'\rightarrow E)$, which is associated with P_1 is equal to $3\bar{\mu}_0$.

See Reference 12 for more details about DOT IV.

Appendix C

CALCULATIONAL PARAMETERS

C.1 Atom Densities

Using the given specifications, the atom densities of all the important nuclides in each of the materials encountered in the VENUS configuration were determined.

Table C-1 contains the atom densities for the fuel elements and Tables C-2 and C-3 correspond to the atom densities for the claddings of the 4.0% and 3.3% fuel types respectively. The atom densities of the pyrex rod and its cladding are shown in Tables C-4 and C-5 respectively. For the baffle and the moderator, Tables C-6 and C-7 show the respective atom densities. Finally, the atom densities of the homogenized fuel cells (for the 4.0% and 3.3% fuel types) and the homogenized pyrex cell are given in Table C-8 and C-9 respectively.

C.2 Reactor Parameters

The Dancoff factors for the 4.0% and 3.3% fuel types were calculated as C = 0.2701 and C = 0.2617 respectively.

The infinite multiplication factors obtained for the 4.0% and 3.3% fuel pins, and the pyrex are K_∞ = 1.3142, K_∞ = 1.3834, and K_∞ = 1.2490 respectively.

Table C-10 shows the critical radius calculated for each of the zones used in the one-dimensional calculations of the VENUS configuration. Each radius is measured from the center of the cylindrical model to the zone's outer boundary.

The critical height of the one-dimensional cylindrical model that was used in a buckling correction is H = 67.44 cm.

C.3 Calculation of Diffusion Coefficients and DB^2

The diffusion coefficients in the leakage terms were calculated from the expression:

$$D_{z,g} = \frac{1}{3\sum_{tr}^{z,g}} \qquad \text{(C-1)}$$

where: $D_{z,g} \equiv$ diffusion coefficient for group g in zone z

$\sum_{tr}^{z,g} \equiv$ macroscopic transport cross-section for group g in zone z

But $$\sum_{tr}^{z,g} = \sum_{T}^{z,g}(P_o) - \frac{1}{3}\sum_{g\to g}^{z,g}(P_1) \qquad \text{(C-2)}$$

where: $\sum_{T}^{z,g}(P_o) \equiv$ total macroscopic cross-section associated with the P-zero component

$\sum_{g\to g}^{z,g}(P_1)$ ≡ macroscopic scattering cross-section associated with the P-one component

Using the above expressions, a home-made computer program of Fig. C-1 was developed, and subsequently employed in calculating the diffusion coefficients and DB^2 values. Table C-11 and C-12 show the diffusion coefficients determined for each zone in the 10 group and 56 group two-dimensional X-Y calculations respectively. The corresponding DB^2 values for the 10 group and 56 group calculations can be found in Tables V-3 and C-13 respectively. A buckling value of $B = 24 \times 10^{-4}$ (cm^{-2}) which was obtained from Mol, was used in the axial leakage (DB^2) calculations.

```
      DIMENSION CS0(100,100),CS1(100,100),CS2(100,100),CS3(100,100)
      DIMENSION XS(100),SIGTR(100),D(100),DB2(100),TITLE(12)
      READ(5,1)IGM,IHM,NMIX,B2
1     FORMAT(3I10,F10.4)
C  DO LOOP FOR MIXTURE
      DO 10 K=1,NMIX
      WRITE(6,50)K
50    FORMAT('1',10X,'DIFFUSION COEF. AND DB SQ FOR MIXTURE #',1X,I3,/)
      WRITE(6,60)
60    FORMAT(10X,'GROUP',15X,'D(CM)',15X,'DBSQ(1/CM)',/)
C  READ THE CROSS SECTION WITH THE P-ZERO COMPONENT
      READ(1)
      READ(1) ((CS0(I,J),I=1,IHM),J=1,IGM)
C  READ THE CROSS SECTION WITH THE P-ONE COMPONENT
      READ(1)
      READ(1) ((CS1(I,J),I=1,IHM),J=1,IGM)
C  READ THE CROSS SECTION WITH THE P-TWO COMPONENT
      READ(1)
      READ(1) ((CS2(I,J),I=1,IHM),J=1,IGM)
C  READ THE CROSS SECTION WITH THE P-THREE COMPONENT
      READ(1)
      READ(1) ((CS3(I,J),I=1,IHM),J=1,IGM)
C  DO LOOP FOR ENERGY GROUP
      DO 20 J=1,IGM
C  IDENTIFY THE POSITION PRECEEDING THE SELF SCATTER GROUP
      M=5
C  INITIALIZE SUM OF SCATTERING CROSS SECTION TO ZERO
      XS(J)=0.0
C  DO LOOP FOR ADDING SELF SCATTER AND DOWN SCATTER TO SUM
      DO 30 I=J,IGM
      M=M+1
30    XS(J)=XS(J)+CS1(M,I)
C  CALCULATE TRANSPORT CROSS SECTION FOR THE GROUP
      SIGTR(J)=CS0(5,J)-XS(J)/3.0
C  CALCULATE THE DIFFUSION COEFFICIENT FOR THE GROUP
      D(J)=1.0/(3.0*SIGTR(J))
C  CALCULATE DB SQUARED
      DB2(J)=D(J)*B2
C  PRINT THE DIFFUSION COEFFICIENTS AND DB SQUARED VALUES
      WRITE(6,70)J,D(J),DB2(J)
70    FORMAT(11X,I3,15X,F10.4,15X,F10.4)
20    CONTINUE
      CALL FFPUN(DB2,IGM,NMIX)
10    CONTINUE
      STOP
      END
```

Note: IGM ≡ # of energy groups
IHM ≡ table length
NMIX ≡ # of mixture
B2 ≡ B^2 value

Fig. C-1. Home-Made Program to Calculate D and DB^2.

Table C-1. Atom Densities for the Fuel Elements

Characteristics	4.0% Fuel Type	3.3% Fuel Type
$A = \pi r^2 (cm^2)$	6.25754E-01	5.26814E-01
$\rho_e (\frac{gm}{cm^3})$	10.21168	10.25029
$N_{U-Total} (\frac{atoms}{barn-cm})$	2.27772E-02	2.28633E-02
$N_{U-234} (\frac{atoms}{barn-cm})$	7.18300E-06	6.74455E-06
$N_{U-235} (\frac{atoms}{barn-cm})$	9.27911E-04	7.65580E-04
$N_{U-236} (\frac{atoms}{barn-cm})$	5.28400E-06	3.68959E-06
$N_{U-238} (\frac{atoms}{barn-cm})$	2.18515E-02	2.20995E-02
$N_{O-16} (\frac{atoms}{barn-cm})$	4.55544E-02	4.57262E-02

Table C-2. Atom Densities for the SS-304 Cladding of 4.0% Fuel

SS-304 Elements	Chemical Composition w/0	$\rho_e (\frac{gm}{cm^3})$	$N (\frac{atoms}{barn-cm})$
Mn	1.29 ± 0.03	7.891	1.11600E-03
Cr	18.3 ± 0.4	7.891	1.67273E-02
Ni	10.03 ± 0.20	7.891	8.11960E-03
Fe	70.038 ± 0.711	7.891	5.96045E-02

Table C-3. Atom Densities for the Zircaloy Cladding of 3.3% Fuel

Zircaloy-4 Elements	Chemical Composition (w/0)	$\rho_e(\frac{gm}{cm^3})$	$N(\frac{atoms}{barn-cm})$
Sn	1.41 ± 0.06	6.6456	4.75500E-04
Zr	98.17 ± 0.06	6.6456	4.30760E-02

Table C-4. Atom Densities for the Pyrex Rod

Elements	Isotopic Composition	(w/o) or (a/o)	$N(\frac{atoms}{barn-cm})$
Si	Natural	100	1.75000E-02
B	B-10	19.775 ± 0.005	1.11430E-03
	B-11	80.225 ± 0.005	4.52070E-03
Al	Natural	100	5.80400E-04
Fe	Natural	100	8.40000E-06
Na	Natural	100	1.48630E-03
K	Natural	100	3.21200E-04
^{0}Total	Natural	100	4.52394E-02

Table C-5. Atom Densities for the SS-304 Pyrex Cladding

SS-304 Elements	Chemical Composition (w/0)	$\rho_e(\frac{gm}{cm^3})$	$N(\frac{atoms}{barn\text{-}cm})$
Mn	0.87 ± 0.42	7.9 ± 0.1	7.53500E-04
Cr	18.4 ± 0.1	7.9 ± 0.1	1.68379E-02
Ni	9.5 ± 0.5	7.9 ± 0.1	7.69930E-03
Fe	70.84 ± 1.28	7.9 ± 0.1	6.03558E-02

Table C-6. Atom Densities for the SS-304 Baffle

SS-304 Elements	Chemical Composition (w/0)	$\rho_e(\frac{gm}{cm^3})$	$N(\frac{atoms}{barn\text{-}cm})$
Mn	1.371 ± 0.441	7.902 ± 0.004	1.18770E-03
Cr	16.37 ± 0.23	7.902 ± 0.004	1.49840E-02
Ni	8.72 ± 0.15	7.902 ± 0.004	7.06890E-03
Fe	72.745 ± 0.343	7.902 ± 0.004	6.19945E-02

Table C-7. Atom Densities for H_2O

Water Elements	$\rho_e(\frac{gm}{cm^3})$	$N(\frac{atoms}{barn\text{-}cm})$
H	1.0	6.68652E-02
O	1.0	3.34326E-02

Table C-8. Atom Densities for the Homogenized Fuel Cells

Composition		N($\frac{\text{atoms}}{\text{barn-cm}}$) 4.0% Fuel Type	3.3% Fuel Type
Fuel	U-234	2.83120E-06	2.22330E-06
	U-235	3.65740E-04	2.54040E-04
	U-236	2.08270E-06	1.22780E-06
	U-238	8.61280E-03	7.33343E-03
	O	1.79550E-02	1.51735E-02
SS-304 Cladding	Mn	7.88830E-05	--
	Cr	1.18235E-03	--
	Ni	5.73925E-04	--
	Fe	4.21310E-03	--
Zircaloy-4 Cladding	Sn	--	4.78945E-05
	Zr	--	4.33881E-03
H_2O Moderator	H	3.52260E-02	3.70110E-02
	O	1.76130E-02	1.85055E-02
	O_{Total}	3.55680E-02	3.36790E-02

Table C-9. Atom Densities for the Homogenized Pyrex Cell

Composition		$N(\frac{atoms}{barn\text{-}cm})$
	Si	3.91030E-03
	B-10	2.48980E-04
	B-11	1.01010E-03
Pyrex	Al	1.29690E-04
	Fe	1.87690E-06
	Na	3.32105E-04
	K	7.17700E-05
	O	1.01085E-02
	Mn	2.71684E-05
SS-304	Cr	6.07112E-04
Cladding	Ni	2.77610E-04
	Fe	2.17621E-03
H_2O	H	3.52260E-02
	O	1.76130E-02
	O_{Total}	2.77215E-02
	Fe_{Total}	2.17809E-03

Table C-10. Critical Radii for the VENUS 1-D Model

Zone	Radius (cm)
1	4.2508
2	7.1088
3	9.6288
4	21.3264
5	34.4184
6	35.4264
11	35.6784
12	35.9304
13	36.1824
14	36.4344
15	36.6864
16	36.9384
7	39.7964
8	48.2830
9	53.2500
10	64.7684

Table C-11. Calculated 10 Group Diffusion Coefficients

	$D_{z,g}$ (cm)			
	Zones			
Group	1,15-18,20 (H_2O)	3,4-10 (3.3% Fuel + Pyrex)	11-13,21-26 (4.0% Fuel)	2,14,19 (SS-304)
1	2.2434	2.3064	2.1771	1.7390
2	1.0544	1.1631	1.1600	1.7191
3	0.5936	0.6935	0.6968	0.9678
4	0.4181	0.5104	0.4947	0.4890
5	0.3870	0.4917	0.4731	0.3898
6	0.3879	0.4949	0.4605	0.3203
7	0.3851	0.4802	0.4494	0.3734
8	0.3686	0.4734	0.4454	0.3662
9	0.3334	0.4609	0.4357	0.3550
10	0.1324	0.2334	0.2267	0.3161

Table C-12. Calculated 56 Group Diffusion Coefficients

	$D_{z,g}$ (cm)			
	Zones			
Group	1,15-18,20 (H_2O)	3,4-10 (3.3% Fuel + Pyrex)	11-13 (4.0% Fuel)	2,14,19 (SS-304)
1	7.5008	4.4858	4.0506	2.3637
2	7.0258	4.3112	3.9175	2.3995
3	5.8587	3.8070	3.4732	2.3432
4	6.1662	3.9361	3.5881	2.3110
5	6.0367	3.8881	3.5470	2.2538
6	5.5458	3.6887	3.3687	2.2021
7	5.7308	3.7730	3.4469	2.1478
8	5.0142	3.4237	3.1467	2.0938
9	5.7221	3.7641	3.4465	2.0140
10	4.9375	3.4180	3.1242	1.8797
11	4.3262	3.1351	2.8785	1.7998
12	3.3303	2.5844	2.3880	1.7496
13	2.9988	2.3797	2.1994	1.7354
14	4.0100	3.0508	2.7985	1.7062
15	3.8991	2.9777	2.7405	1.6780
16	3.9077	2.9827	2.7269	1.5426
17	4.5454	3.3590	3.0874	1.6278
18	5.2304	3.7700	3.5494	1.8633
19	3.8827	3.0189	2.8057	1.7197
20	3.1645	2.5523	2.3747	1.6739
21	2.9749	2.4453	2.2727	1.6122

Table C-12. Continued

	$D_{z,g}$ (cm)			
	Zones			
Group	1,15-18,20 (H_2O)	3,4-10 (3.3% Fuel + Pyrex)	11-13 (4.0% Fuel)	2,14,19 (SS-304)
21	2.9749	2.4453	2.2727	1.6122
22	2.3235	1.9887	1.8725	1.7684
23	2.5436	2.1646	2.0436	1.7883
24	2.2690	1.9786	1.8564	1.5709
25	2.2182	1.9501	1.8547	1.6893
26	1.7762	1.6042	1.5303	1.5916
27	1.4610	1.3427	1.2995	2.0597
28	1.2341	1.1227	1.1041	2.2789
29	1.6912	1.5268	1.5279	2.0505
30	1.7228	1.5535	1.5294	1.3878
31	1.6747	1.5221	1.5499	2.0440
32	1.5925	1.4391	1.4796	1.8707
33	8.6454	0.8153	0.8068	1.3082
34	1.0331	0.9740	0.9852	1.8614
35	1.0250	0.9786	0.9863	1.4147
36	0.9715	0.9423	0.9261	0.8945
35	0.8962	0.8885	0.8897	1.1490
38	0.8300	0.8376	0.8125	0.7025
39	0.8066	0.8200	0.8012	0.7479
40	0.7740	0.7950	0.7991	1.0437

Table C-12. Continued

Group	$D_{z,g}$(cm) Zones 1,15-18,20 (H_2O)	3,4-10 (3.3% Fuel + Pyrex)	11-13 (4.0% Fuel)	2,14,19 (SS-304)
41	0.7211	0.7519	0.7407	0.7925
42	0.6836	0.7238	0.6993	0.5934
43	0.6641	0.7074	0.6267	0.2643
44	0.6513	0.6970	0.7121	1.6934
45	0.6455	0.6923	0.7030	1.4453
46	0.6329	0.6819	0.6680	0.7235
47	0.6190	0.6700	0.6404	0.5259
48	0.6074	0.6599	0.6102	0.3757
49	0.5990	0.6450	0.5863	0.3067
50	0.5932	0.6166	0.5792	0.3280
51	0.5891	0.6017	0.5917	0.3943
52	0.5864	0.6397	0.5742	0.3496
53	0.5818	0.6458	0.5867	0.3582
54	0.5800	0.6476	0.5842	0.3739
55	0.5781	0.6605	0.5964	0.3654
56	0.5602	0.2431	02313	0.3013

Table C-13. Calculated 56 Group Axial Leakage Approximation Values

	$[DB^2]_{z,g}$ (cm^{-1})			
	Zones			
Group	1,15-18,20 (H_2O)	3,4-10 (3.3% Fuel + Pyrex)	11-13 (4.0% Fuel)	2,14,19 (SS-304)
1	1.8002E-02	1.0766E-02	9.7214E-03	5.6730E-03
2	1.6862E-02	1.0347E-02	9.4019E-03	5.7589E-03
3	1.4061E-02	9.1368E-03	8.3358E-03	5.6237E-03
4	1.4799E-02	9.4466E-03	8.6115E-03	5.5465E-03
5	1.4488E-02	9.3314E-03	8.5129E-03	5.4092E-03
6	1.3310E-02	8.8528E-03	8.0849E-03	5.2850E-03
7	1.3754E-02	9.0553E-03	8.2725E-03	5.1548E-03
8	1.2034E-02	8.2169E-03	7.5522E-03	5.0252E-03
9	1.3733E-02	9.0339E-03	8.2715E-03	4.8336E-03
10	1.1850E-02	8.2032E-03	7.4981E-03	4.5113E-03
11	1.0383E-02	7.5242E-03	6.9085E-03	4.3196E-03
12	7.9927E-03	6.2025E-03	5.7312E-03	4.1991E-03
13	7.1972E-03	5.7113E-03	5.2786E-03	4.1649E-03
14	9.6241E-03	7.3220E-03	6.7165E-03	4.0950E-03
15	9.3578E-03	7.1465E-03	6.5772E-03	4.0273E-03
16	9.3784E-03	7.1586E-03	6.5446E-03	3.7022E-03
17	1.0909E-02	8.0616E-03	7.4097E-03	3.9067E-03
18	1.2553E-02	9.0481E-03	8.5186E-03	4.4719E-03
19	9.3185E-03	7.2454E-03	6.7336E-03	4.1273E-03
20	7.5947E-03	6.1256E-03	5.6993E-03	4.0173E-03

Table C-13. (Continued)

	$[DB^2]_{z,g}$ (cm^{-1})			
	Zones			
Group	1,15-18,20 (H_2O)	3,4-10 (3.3% Fuel + Pyrex)	11-13 (4.0% Fuel)	2,14,19 (SS-304)
21	7.1398E-03	5.8687E-03	5.4545E-03	3.8692E-03
22	5.5765E-03	4.7729E-03	4.4940E-03	4.2442E-03
23	6.1046E-03	5.1950E-03	4.9046E-03	4.2920E-03
24	5.4456E-03	4.7487E-03	4.4553E-03	3.7701E-03
25	5.3238E-03	4.6802E-03	4.4512E-03	4.0544E-03
26	4.2629E-03	3.8502E-03	3.6728E-03	3.8199E-03
27	3.5065E-03	3.2224E-03	3.1188E-03	4.9434E-03
28	2.9618E-03	2.6945E-03	2.6498E-03	5.4693E-03
29	4.0590E-03	3.6643E-03	3.6669E-03	4.9211E-03
30	4.1347E-03	3.7283E-03	3.6706E-03	3.3307E-03
31	4.0193E-03	3.6531E-03	3.7198E-03	4.9056E-03
32	3.8221E-03	3.4538E-03	3.5510E-03	4.4897E-03
33	2.0749E-03	1.9567E-03	1.9364E-03	3.1398E-03
34	2.4794E-03	2.3377E-03	2.3646E-03	4.4674E-03
35	2.4601E-03	2.3486E-03	2.3671E-03	3.3954E-03
36	2.3317E-03	2.2615E-03	2.2226E-03	2.1469E-03
37	2.1510E-03	2.1324E-03	2.1354E-03	2.7575E-03
38	1.9920E-03	2.0103E-03	1.9500E-03	1.6860E-03
39	1.9358E-03	1.9681E-03	1.9229E-03	1.7949E-03
40	1.8576E-03	1.9081E-03	1.9179E-03	2.5050E-03

Table C-13. (Continued)

Group	$[DB^2]_{z,g}$ (cm^{-1})			
	Zones			
	1,15-18,20 (H_2O)	3,4-10 (3.3% Fuel + Pyrex)	11-13 (4.0% Fuel)	2,14,19 (SS-304)
41	1.7307E-03	1.8045E-03	1.7776E-03	1.9019E-03
42	1.6407E-03	1.7371E-03	1.6784E-03	1.4242E-03
43	1.5938E-03	1.6978E-03	1.5040E-03	6.3442E-04
44	1.5632E-03	1.6727E-03	1.7091E-03	4.0642E-03
45	1.5493E-03	1.6615E-03	1.6871E-03	3.4688E-03
46	1.5189E-03	1.6365E-03	1.6031E-03	1.7365E-03
47	1.4855E-03	1.6079E-03	1.5370E-03	1.2621E-03
48	1.4577E-03	1.5837E-03	1.4645E-03	9.0158E-04
49	1.4375E-03	1.5481E-03	1.4071E-03	7.3614E-04
50	1.4236E-03	1.4798E-03	1.3901E-03	7.8722E-04
51	1.4138E-03	1.4442E-03	1.4201E-03	9.4641E-04
52	1.4074E-03	1.5352E-03	1.3780E-03	8.3906E-04
53	1.3963E-03	1.5500E-03	1.4081E-03	8.5960E-04
54	1.3921E-03	1.5543E-03	1.4021E-03	8.9737E-04
55	1.3875E-03	1.5852E-03	1.4314E-03	8.7693E-04
56	1.3446E-03	5.8339E-04	5.5521E-04	7.2317E-04

VITA

Paul O. Morakinyo was born in 1956 in Ibadan, Nigeria, W. Africa. He was raised by his parents under a Christian and disciplined background. He had both his elementary and high school education in Nigeria.

In September 1976, he began an Electrical Engineering program at the University of Windsor, Ontario, Canada, where he graduated with a Bachelor of Applied Science degree in 1980.

He entered Louisiana State University in 1981 to pursue a Master's degree in Electrical Engineering, with specialization in Power Systems. After graduation in 1982, he decided to seek a Master's degree in Nuclear Engineering to complement his energy conscious field. Upon graduation, he hopes to either seek full employment with a utility company, or embark on a Ph.D. program.